

## Flow Patterns around Dark Matter Halos: the Link between Halo Dynamical Properties and Large Scale Tidal Field

Jingjing Shi<sup>1,2</sup>, Huiyuan Wang<sup>1</sup> and H.J. Mo<sup>3</sup>

jingssrs1989@gmail.com; whywang@mail.ustc.edu.cn; hjmo@astro.umass.edu

### ABSTRACT

We study how halo intrinsic dynamical properties are linked to their formation processes for halos in two mass ranges,  $10^{12} - 10^{12.5} h^{-1} M_{\odot}$  and  $\geq 10^{13} h^{-1} M_{\odot}$ , and how both are correlated with the large scale tidal field within which the halos reside at present. Halo merger trees obtained from cosmological  $N$ -body simulations are used to identify infall halos that are about to merge with their hosts. We find that the tangential component of the infall velocity increases significantly with the strength of the local tidal field, but no strong correlation is found for the radial component. These results can be used to explain how the internal velocity anisotropy and spin of halos depend on environment. The position vectors and velocities of infall halos are aligned with the principal axes of the local tidal field, and the alignment depends on the strength of the tidal field. Opposite accretion patterns are found in weak and strong tidal fields, in the sense that in a weak field the accretion flow is dominated by radial motion within the local structure, while a large tangential component is present in a strong field. These findings can be used to understand the strong alignments we find between the principal axes of the internal velocity ellipsoids of halos and the local tidal field, and their dependence on the strength of tidal field. They also explain why halo spin increases with the strength of local tidal field, but only in weak tidal fields does the spin-tidal field alignment follow the prediction of the tidal torque theory. We discuss how our results may be used to understand the spins of disk galaxies and velocity structures of elliptical galaxies and their correlations with large-scale structure.

*Subject headings:* dark matter - large-scale structure of the universe - galaxies: halos - methods: statistical

---

<sup>1</sup>Key Laboratory for Research in Galaxies and Cosmology, Department of Astronomy, University of Science and Technology of China, Hefei, Anhui 230026, China

<sup>2</sup>SISSA, Via Bonomea 265, I-34136 Trieste, Italy

<sup>3</sup>Department of Astronomy, University of Massachusetts, Amherst MA 01003-9305, USA

## 1. Introduction

In the standard cold dark matter (CDM) paradigm of structure formation, a key concept is the formation and evolution of dark matter halos. The halo properties, such as internal structures, dynamical properties, assembly histories and clustering properties, and the correlations among them have been studied in great detail (see Mo et al. 2010, for an overview). Since halos are the hosts of observed galaxies, these studies are essential for understanding the formation and evolution of galaxies in the cosmic density field.

One particular property of the CDM halo population is that the spatial clustering of halos of a given mass depends significantly on various halo properties. Gao et al. (2005) and Li et al. (2008) found that old low-mass halos are more strongly clustered than their younger counterparts. Halo clustering also depends on halo structural properties, such as halo concentration and substructure abundance (Wechsler et al. 2006; Jing et al. 2007), and on dynamical properties, such as halo angular momentum (Bett et al. 2007; Gao & White 2007), and internal velocity structure (Faltenbacher & White 2010). All these dependencies, usually referred to as assembly bias, indicate the importance of environmental effects on halo formation and evolution.

Attempts have been made to understand the environmental effects on halo properties from various perspectives (Wang et al. 2007; Sandvik et al. 2007; Keselman & Nusser 2007; Desjacques 2008; Dalal et al. 2008; Fakhouri & Ma 2009; Lacerna & Padilla 2011, 2012; Li et al. 2013). These studies found that old low-mass halos usually reside in the vicinity of big structures, and suggested that their accretion may be suppressed or even truncated by the large scale tidal field. Wang et al. (2011) studied the correlations between a number of halo properties and the tidal field, and found significant correlations between the local tidal fields and all the halo properties they studied, including half-mass assembly time, spin, axis ratio, and substructure abundance. In particular, they found that the tidal field is the primary environmental effect shaping most of the halo intrinsic properties, while other commonly used environmental indicators, such as the local mass density and the morphology of the large scale structure, are secondary in that their effects operate mainly through their correlations with the tidal field. However, a detailed understanding of how environmental effects shape the structure and dynamics of dark matter halos is still lacking.

In the CDM paradigm of structure formation, dark matter halos form through the accretion (merger) of smaller halos, and halo properties are expected to be determined by their formation histories. So far, only a small number of simple quantities have been adopted to characterize the formation histories of individual halos, and most of them are based on characteristic times at which a halo has assembled a fixed fraction of its final mass (e.g. Navarro et al. 1995; Wechsler et al. 2002; Zhao et al. 2009) or the gravitational potential well associated with the halo has reached some depth (Zhao et al. 2003). On the basis of these formation times, it has been shown that younger halos on average are less concentrated and more elongated, spin faster, and contain a larger amount of substructures, than their older counterparts of the same mass (e.g. Gao et al. 2004; Allgood et al. 2006; Hahn et al. 2007; Wang et al. 2011). However, the formation histories

of individual halos are complex and cannot be described completely by these simple characteristic formation times. Indeed, information about how small halos to be accreted (i.e. infall halos) are distributed in phase space is totally lost in these characteristic formation times, and yet may be pivotal in the understanding of the structural and dynamical properties of the halos that grow through such accretion process. Previous studies have found that infall halos on average have higher radial than tangential velocities (Tormen 1997; Vitvitska et al. 2002; Benson 2005; Wang et al. 2005; Wetzel 2011; Jiang et al. 2014). Such anisotropic orbits of accretion may affect the internal velocity structure of the descendant halos that form through such accretion. Indeed, dark matter halos in  $N$ -body simulations are found to be dominated by radial orbits in their internal velocity distributions, at least in the outer parts (Colín et al. 2000; Rasia et al. 2004; Ludlow et al. 2011; Sparre & Hansen 2012). Clearly, it is important to understand and quantify such links between halo internal properties and their accretion processes. Furthermore, since the phase space distribution of halos to be accreted into a host halo is expected to be closely linked to the large-scale environment within which the host halo resides, such information is also crucial in order to understand the environmental effects on halo structure and dynamics.

In this paper, we study in detail how small halos are accreted by their hosts, how the properties of the host halos are determined by the accretion process, and how the accretion processes, through which the intrinsic properties of halos are determined, are linked to the local environments of the halos. We pay particular attention to halo dynamical properties, such as velocity dispersion, angular momenta and velocity ellipsoid. The structure of the paper is organized as follows. In Section 2, we describe the simulations we use, and our methods for halo identification, merger tree construction and tidal field estimation. In Section 3, we investigate the orbital distributions of infall halos and their dependencies on the large scale tidal field. Section 4 examines how halo dynamical properties depend on environments, and how the dependence can be understood in terms of the orbits of infall halos. Finally, in Section 5 we discuss and summarize our main results.

## 2. Numerical Simulations and Dark Matter Halos

### 2.1. Simulation and Halo Identification

In this study, we use two  $N$ -body cosmological simulations carried out with Gadget-2 (Springel 2005). These simulations adopted a flat  $\Lambda$ CDM cosmological model, with  $\Omega_{\Lambda,0} = 0.742$  for the cosmological constant,  $\Omega_{\text{dm},0} = 0.214$  and  $\Omega_{\text{b},0} = 0.044$  for CDM and baryons, respectively,  $h = 0.72$  for the dimensionless value of the Hubble constant,  $\sigma_8 = 0.8$  for the *rms* linear mass fluctuation in a sphere of radius  $8 h^{-1}\text{Mpc}$  extrapolated to  $z = 0$ , and  $n = 1$  for the slope of the primordial fluctuation spectrum. The CDM density field of each simulation is traced by  $1024^3$  particles, each with mass  $m_{\text{p}} \approx 5.3352 \times 10^8 h^{-1}M_{\odot}$ , from  $z = 72$  to  $z = 0$  in a cubic box of a side length  $200 h^{-1}\text{Mpc}$ . The gravitational force is softened isotropically on a co-moving length scale of  $4 h^{-1}\text{kpc}$  (Plummer equivalent). Each simulation outputs 80 snapshots from  $z = 17$  to  $z = 0$ ,

equally spaced in the logarithm of the expansion factor.

Dark matter halos are identified using the standard friends-of-friends (hereafter FOF) algorithm (Davis et al. 1985) with a link length that is 0.2 times the mean inter-particle separation. We only consider halos that contain at least 20 particles, and the mass of a halo is the sum of the masses of all particles in the halo. It is known that some FOF halos, in particular small ones containing small number of particles, may be dominated by ‘fuzzy’ particles that are not gravitationally bound. We use SUBFIND algorithm developed by Springel et al. (2001) to identify subhalos that are gravitationally bound. If the most massive bound structure contains less than half of the total mass of the FOF halo, this FOF halo is considered to be dominated by ‘fuzzy’ particles and is excluded from our analysis.

## 2.2. Merger Trees and Halos to be Accreted

Here we give a brief description of the construction of halo merger trees and the identification of halos to be accreted into a host halo. We identify dark matter halos using the method described above in each of the snapshots and cross link halo particles in adjacent snapshots. If more than half of the particles in a halo (denoted as halo ‘A’) end up in a halo in the next snapshot (denoted as halo ‘B’), we call halo ‘A’ a progenitor of halo ‘B’, and halo ‘B’ the descendant of ‘A’. This definition ensures that a halo can have one or more progenitors but can only have one descendant. The uniqueness of the descendant allows us to build up a unique merger tree for every halo at present day. For any halo identified at a given time, its most massive progenitor in the last snapshot is referred to as its main progenitor. Tracing the main progenitors back in time gives the main trunk of the merger tree of a halo identified at  $z = 0$ .

For a given halo at present day, we select all of its progenitors that are not parts of the main trunk but whose first generation descendants are main trunk halos. These halos are referred to as infall halos. The main progenitors, into which these infall halos are falling, are called host halos. The redshift at which an infall halo is identified is referred to as the infall redshift,  $z_{\text{inf}}$ , of the infall halo. Infall halos are therefore merging with their hosts at a redshift around  $z_{\text{inf}}$ . Some infall halos may have been sub-halos of their hosts at  $z > z_{\text{inf}}$  but have later moved outside of their hosts and are now falling back onto the hosts. The orbits of these halos may have been severely altered by interactions with the internal structures of the hosts, and so are not suitable for our investigation of large-scale environmental effects. Unfortunately, such halos cannot be directly identified because our merger trees constructed by using FOF halos cannot trace the evolution of subhalos within host halos. As an approximation, we adopt the method developed in Wang et al. (2009a) to identify these halos. For an infall halo ‘A’, we trace its main progenitor back in time until its earliest main progenitor ‘B’ is found in a snapshot, say  $n$ . We then check whether or not more than half of the particles of halo ‘B’ belong to the main progenitor of the host halo of ‘A’ at an earlier snapshot  $n - 1$ . If yes, then ‘A’ is considered to have been ejected by the host at an early time, and is excluded from our analysis. Thus, we only consider halos that are in their first infall.

A tiny fraction of infall halos are not contained in their host halos at  $z = 0$  (Ludlow et al. 2009; Wang et al. 2009a; Bahé et al. 2012; Li et al. 2013). They are either ejected by their hosts after being accreted or flybys fortuitously linked to their massive neighbors by the FOF algorithm. This population may have important implications for understanding the existence of quenched galaxies near clusters and groups in the local Universe (Wang et al. 2009b; Li et al. 2013; Wetzel et al. 2014). To study the environmental dependence of halo assembly in detail, we identify this population in the following way. If more than half of the particles in an infall halo are not contained in its host (or descendant) at  $z = 0$ , the infall halo is thought to have finally escaped. This population will be referred to as ejected halos. Other infall halos, which stay as subhalos within their hosts at  $z = 0$ , are referred to as the staying population.

Limited by finite mass resolution and small number statistics, here we focus on the merger histories of host halos in two mass ranges,  $10^{12.5} \geq M_0 \geq 10^{12} h^{-1} M_\odot$  (Milk Way size) and  $M_0 \geq 10^{13} h^{-1} M_\odot$  (massive group size), where  $M_0$  is the halo mass at  $z = 0$ . The total numbers of host halos in the two mass ranges are listed in Table 1. For the host halos in the lower mass bin, infall halos with masses  $M_{\text{inf}}$  given by  $M_{\text{inf}}/M_0 \geq 20m_p/10^{12} \simeq 0.01$  are taken into account. These infall halos are divided into two samples. The first sample, denoted by M12(S), consists of only staying infall halos. The second, M12(E), contains infall halos that eventually are ejected by their hosts. The infall halos of the massive hosts are divided into four samples. The first, M13(S), consists of all infall halos with  $M_{\text{inf}}/M_0 \geq 0.01$  in the staying population. The mass threshold adopted here is the same as that for M12(S), and so one can investigate the dependence on host halo mass by comparing M12(S) and M13(S). The second, M13(S'), consists of infall halos with  $0.01 > M_{\text{inf}}/M_0 \geq 20m_p/10^{13} \simeq 0.001$ , again in the staying population. A comparison between M13(S) and M13(S') may help us to understand the dependence on the mass of infall halos. The third and fourth samples, M13(E) and M13(E'), contain infall halos of the ejected population, with masses in the same ranges as for M13(S) and M13(S'), respectively. The numbers of infall halos in all the six samples are listed in Table 1.

Figure 1 shows the distributions of  $z_{\text{inf}}$  for the six infall halo samples described above. M12(S) on average has higher  $z_{\text{inf}}$  than M13(S), as expected from the fact that smaller halos are, on average,

Table 1: Number of host halos and infall halos in the samples.  $M_0$  is the mass of host halos at  $z = 0$ , in unit of  $h^{-1} M_\odot$ ,  $N_h$  is the number of host halos at  $z = 0$ .  $N_{\text{inf}}$  is the number of infall halos. Low  $z_{\text{inf}}$  indicates  $z_{\text{inf}} \leq 0.4$  and high  $z_{\text{inf}}$  indicates  $0.75 \leq z_{\text{inf}} \leq 1.25$ .

$\log M_0$	$\geq 13$				12 - 12.5	
$N_h$	5793				37124	
Infall halo	M13(S')	M13(S)	M13(E')	M13(E)	M12(S)	M12(E)
$N_{\text{inf}}$	214720	49503	37014	1718	330221	30818
$z_{\text{inf}}$	low	high	low	high		
$N_{\text{inf}}$	54088	38251	12135	9772		
					low	high
					56767	55946

older than more massive ones. Infall halos that stay as sub-halos are accreted over a wide range of redshift. In order to minimize possible dependence on redshift, we consider infall halos accreted in two relatively narrow redshift ranges, a low-redshift range  $z_{\text{inf}} \leq 0.4$  and a high redshift range,  $0.75 \leq z_{\text{inf}} \leq 1.25$ . The numbers of halos in these two redshift bins for samples M12(S), M13(S) and M13(S') are also listed in Table 1. The distributions of the ejected halos are much narrower, with peaks at  $z \sim 0.5$ , and the majority of such halos have infall redshifts below  $z = 1$ . Because of this we do not split ejected halos further according to infall redshifts.

### 2.3. Large Scale Tidal Field

A number of quantities can be used to characterize the large scale environment of dark matter halos, including halo bias parameter, local mass over-density, morphology of large scale structure (i.e. cluster, filament, sheet and void), velocity shear field and large scale tidal field (Mo & White 1996; Gao et al. 2005; Maulbetsch et al. 2007; Hahn et al. 2007; Wang et al. 2011; Libeskind et al. 2013a, 2014a). In this paper, we adopt the (external) tidal field at the location of a halo to represent the large-scale environment in which the halo resides. The (external) tidal field is estimated by summing up the tidal forces exerting on the halo by all other halos above a mass threshold,  $M_{\text{th}} = 10^{12} h^{-1} M_{\odot}$ , and is normalized by the self-gravity of the halo in question (Wang et al. 2011). The local tidal field can be characterized by the three eigenvalues of the local tidal tensor,  $t_1$ ,  $t_2$  and  $t_3$  (by definition,  $t_1 > t_2 > t_3$ ), and the corresponding eigenvectors,  $\mathbf{t}_1$ ,  $\mathbf{t}_2$  and  $\mathbf{t}_3$ . The three eigenvalues satisfy  $t_1 + t_2 + t_3 \equiv 0$ , so  $t_1$  is always positive and  $t_3$  is always negative. Thus, the large scale tidal field stretches the material along  $\mathbf{t}_1$  but compresses it along  $\mathbf{t}_3$ . In this paper, we use  $t_1$  as an indicator of the local tidal field strength.

The other method for calculating the tidal field, often adopted in the literature (e.g. Hahn et al. 2007; Zhang et al. 2009), directly makes use of the mass density field to get the *mass tidal field*. As shown in Wang et al. (2011),  $\mathbf{t}_1$ ,  $\mathbf{t}_2$  and  $\mathbf{t}_3$  defined above are tightly aligned with the corresponding eigenvectors of the mass tidal field. Different from the mass tidal field, the tidal field defined above does not include the contribution of the self-gravity of the halo, and therefore is more closely related to the large-scale environment. Moreover, two halos that reside in a similar environment may suffer very differently from the local environment. For example, a ‘hot’ environment for a small halo can be quite ‘cold’ for a massive halo. To take into account this halo mass-dependent effect, our tidal field is normalized by the self-gravity of the halo, so that one can compare the environmental effects for halos of different masses. More details about the tidal field defined here and its correlations with other environmental quantities can be found in the appendix of Wang et al. (2011).

We consider halos accreted at different redshifts. The environmental indicator can be chosen to be either the tidal field within which the  $z = 0$  descendant halo resides or the tidal field when the accretion process occurs. In this paper, we use the tidal field at  $z = 0$  as an environmental indicator. There are two primary reasons for this choice. First, our eventual goal is to study similar effects in observational data (see Section 5). As shown in Yang et al. (2007), galaxy groups properly

selected from large redshift surveys of galaxies can be used to represent the halo population. Dark matter halos are biased tracers of the underlying density field and can be used to estimate the large scale tidal field (Wang et al. 2012). Currently, such a galaxy group catalog is only available at low redshift. Second, one of the purposes of this paper is to use the environmental dependence of halo accretion to interpret the environmental dependence of dynamical properties of halos at  $z = 0$  (Section 4). The local tidal field within which these halos reside provides one such environmental indicator that can be estimated from observation.

One interesting question is how the tidal field around a halo evolves with redshifts. To answer this question, we analyze the alignments and correlations of the external tidal field around a  $z = 0$  halo with those around its main progenitors at  $z = 0.4$  and  $z = 1.0$ . Note that the external tidal field at a high redshift is also calculated without including the contribution of surrounding halos that will end up in the final halo. The results for the alignments and the correlations of  $t_1$  are shown in Figure 2 and 3, respectively. The reason for choosing these two particular redshifts is that our following analyses focus on infall halos in the two redshift ranges,  $z_{\text{inf}} \leq 0.4$  and  $0.75 \leq z_{\text{inf}} \leq 1.25$ . Clearly, the eigenvectors of the tidal fields at both  $z = 0.4$  and  $z = 1.0$  are strongly aligned with the corresponding vectors at  $z = 0$ . The alignments between  $z = 0.4$  and  $z = 0$  are stronger than those between  $z = 1.0$  and  $z = 0$ , and the dependence on halo mass is rather weak. For both halo mass ranges, the tidal field strength at  $z = 0.4$  is tightly correlated with that at  $z = 0$ , and the correlation becomes weaker for  $z = 1.0$ . Overall, the tidal field at  $z = 0$  can be used as a proxy of the tidal field at higher redshift, at least to  $z \sim 1$ , and particularly for the orientation of the tidal field.

### 3. Environmental Dependence of Halo Accretion

In this section, we investigate the environmental dependence of halo accretion from three different aspects. We emphasize again that we use the  $z = 0$  tidal field as our environmental indicator. We first study the mass function of infall halos residing in different environments (Subsection 3.1), and then investigate the correlations between the tidal field and the orbital properties of infall halos (Subsection 3.2). Finally, in Subsection 3.3, we examine the alignment between the position and velocity vectors of infall halos and the local tidal field.

#### 3.1. Infall Halo Mass Function

The infall halo mass function, sometimes also called the un-evolved subhalo mass function in the literature, is often used to study the evolution of subhalos within their hosts (Giocoli et al. 2008; Yang et al. 2011). Here we examine whether the infall halo mass function depends on the large scale environment. To this end we calculate the mean infall mass functions for host halos which are located in regions of the highest, intermediate and lowest 20 percentiles of the  $t_1$

distribution. The results are shown in Figure 4. In each panel, the three dotted lines show the mass functions of staying infall halos, while the dotted lines connecting squares are the results for the ejected population. To ensure completeness, we only use infall halos in samples M12(S) and M12(E) to calculate the mass functions for host halos of  $10^{12.5} \geq M_0 \geq 10^{12.0} h^{-1} M_\odot$ , and samples M13(S)+M13(S') and M13(E)+M13(E') for host halos of  $M_0 \geq 10^{13} h^{-1} M_\odot$ .

The mass functions of infall halos obtained from samples M12(S) and M13(S)+M13(S') are almost independent of  $t_1$ . Since these halos are the ones that will stay in their hosts, they are the major sources of halo growth, in the sense that the integration of the mass function should be roughly equal to one. The mass function is also quite independent of host halo mass, consistent with previous findings (Giocoli et al. 2008). We fit the simulation data with the formula proposed by Giocoli et al. (2008),

$$\frac{dN}{d \ln(m_v/M_0)} = N_0 x^{-\alpha} e^{-6.283x^3}, \quad x = \frac{m_v}{\alpha M_0} \quad (1)$$

where  $m_v$  is set to be  $M_{\text{inf}}$ . The resultant mean fitting lines are shown in the figure for comparison. As one can see, the empirical formula fits our results well, demonstrating the robustness of our merger tree construction. The mean fitting parameters are  $\alpha = 0.67$  (0.68) and  $N_0 = 0.43$  (0.40) for M12(S) [M13(S)+M13(S')]. The slopes  $\alpha$  obtained here are slightly less than  $\alpha = 0.8$  obtained by Giocoli et al. (2008), but the amplitudes are significantly higher than their value,  $N_0 = 0.2$ . The difference may be caused by different cosmological models and the definition of halos in the two analyses.

Different from the staying population, the mass functions for M12(E) and M13(E)+M13(E') strongly depend on the large scale tidal field. The ejected halo population is much more abundant in regions of stronger tidal field, and the difference becomes larger as the infall halo mass increases. At the high mass end, the ejected halo abundance in the 20% highest  $t_1$  regions is about 10 times higher than that at the 20% lowest  $t_1$  regions. This suggests that the large-scale tidal field can affect the accretion of halos, and infall halos in ‘hotter’ (strong tide) environments are more likely to escape from the potential well of their hosts. The slope of the mass function for the ejected halo population is, on average, steeper than the mass function of the staying population, indicating that halos with lower masses are easier to be ejected. Overall, the ejected population is only a small fraction of the total, and the fraction is higher for lower mass host halos (see Table 1).

### 3.2. Orbits of Infall Halos

Since the staying population dominates the total infall halos, we first investigate how their acquisitions by their host halos are affected by environmental effects. Let us first look at  $v_r$  and  $v_\theta$ , the radial and tangential velocities of infall halos relative to the hosts at  $z_{\text{inf}}$ . The radial direction is defined as the position vector of the infall halo relative to the minimum potential position of the host halo; a negative radial velocity means that the halo is moving towards its host. Figure

5 and 6 show, respectively, the probability distributions of  $v_r$  and  $v_\theta$ , both normalized by the circular velocity of the host,  $v_{\text{vir}}$ , at  $z_{\text{inf}}$ , for samples M12(S), M13(S) and M13(S') in the highest, intermediate and lowest 20 percentiles of the  $t_1$  distribution. Results are shown separately for two narrow infall redshift ranges, low ( $z_{\text{inf}} \leq 0.4$ ) and high ( $0.75 \leq z_{\text{inf}} \leq 1.25$ ). As one can see, the  $v_r$  distribution peaks around  $-0.9v_{\text{vir}}$ , while  $v_\theta$  peaks at a smaller value. These results are in qualitative agreement with those obtained before (Benson 2005; Wang et al. 2005; Wetzel 2011; Jiang et al. 2014). The fact that the free-fall velocity near the host virial radius is about  $-v_{\text{vir}}$  suggests that the radial velocity of an infall halo is primarily produced by the gravity of the host. This interpretation is also supported by the similarity between the distributions for host halos of different mass [samples M12(S) versus M13(S)] at different redshifts. A small fraction of halos are moving outward with very low (positive) velocities and are expected to turn back shortly.

The gravity of the host is not the sole factor that affects the velocity distributions of the infall halos. In fact, the distributions also depend on the environments where the hosts reside. First, the average tangential velocity increases as the tidal force increases. As shown in the top left panel, the peak value of the tangential velocity distribution for low redshift M12(S) increases from  $\sim 0.3v_{\text{vir}}$  for the lowest 20% of  $t_1$  to  $\sim 0.6v_{\text{vir}}$  for the highest 20%, in contrast to the peak of the  $v_r$  distribution, which is almost independent of  $t_1$ . Second, the distributions of both  $v_r$  and  $v_\theta$  are broader in a stronger tidal field, and the effect is more significant for radial velocity. Take the low-redshift M12(S) as an example, the dispersion in the  $v_r$  distribution changes from 0.19 to 0.27 and to 0.44 from low  $t_1$  to intermediate  $t_1$  and to high  $t_1$ , while the dispersion in the  $v_\theta$  distribution changes from 0.25 to 0.30 and to 0.32.

The dependence on the tidal strength appears weaker for infall halos at higher redshift. There are two possible reasons for this. First, the tidal field, which is estimated from halos at  $z = 0$ , might not be a good tracer of environments at high redshift. Second, environmental effects are indeed weaker at higher redshift. We will come back to this question later.

Another useful quantity is the infall angle,  $\cos \alpha_{\text{inf}}$ , defined as

$$\cos \alpha_{\text{inf}} = \frac{|v_r|}{\sqrt{v_r^2 + v_\theta^2}}. \quad (2)$$

We split the infall halo sample into several equal-sized subsamples according to their local  $t_1$ , and calculate the mean values of  $\cos \alpha_{\text{inf}}$  and  $t_1$  for each of these subsamples. The results are shown in Figure 7. Note that radial velocity is the dominating component when  $v_r^2 \geq v_\theta^2/2$ , i.e. when  $\cos \alpha_{\text{inf}} \geq 0.58$ . The results clearly show that the accretion flow preferentially moves radially in all environments. Moreover, there is clear dependence of infall angle on the redshift and on the masses of both the infall halo and the host. The accretion flow at high redshift is more dominated by radial motion than at low redshift. This is expected, because environmental effects relative to the self gravity of the hosts are weaker at higher redshift. A comparison between the results for M12(S) and M13(S) suggests that the accretion flow around a more massive host is also more radial.

The infall angle is strongly correlated with the strength of the tidal force,  $t_1$ . As the tidal

force increases, the mean  $\cos \alpha_{\text{inf}}$  decreases significantly for all samples. This is consistent with the velocity distributions shown in Figures 5 and 6. Interestingly, such environmental dependence for infall halos accreted at high redshift ( $z_{\text{inf}} \sim 1$ ) is almost as strong as for those with lower  $z_{\text{inf}}$ . This suggests that the tidal field around a halo at  $z = 0$  is correlated with the tidal field around its main progenitors at high redshifts. As the large-scale structure in the Universe evolves, the strength of the tidal field at the location of a halo is expected to evolve with time. The tidal field obtained from the halo population at  $z = 0$  may serve as an approximation of the *scaled* version of the tidal field at high  $z$  (see Section 2.3 for more discussion).

Finally, let us look at the ejected halo population, whose results are also presented in Figures 5, 6 and 7. Compared to the staying population, the ejected population has slightly higher mean radial velocities, significantly higher tangential velocities and much broader velocity distributions. These results are expected. A higher tangential velocity means that the orbit is both more loosely bound, which makes a final merger less likely, and more circular, which makes orbital decay due to dynamical friction less effective. Both effects make the sub-halo easier to escape from the host. The dependence of the tangential velocity distribution on the tidal field strength is stronger for ejected halos than for the staying ones, as shown in the lower panels of Figure 6, and the dominance of the radial component of the infall velocity also decreases with increasing  $t_1$  more rapidly, as shown in Figure 7.

### 3.3. Alignment of Accretion Flow with Tidal Tensor

The results shown above may suggest that the velocity field of accretion flow is regulated by the local large scale tidal field.<sup>1</sup> Cosmological tidal field is known to be strongly anisotropic: it stretches the accretion flow along the  $\mathbf{t}_1$  direction, while compresses it along  $\mathbf{t}_3$ . This suggests that the spatial distribution and velocity field of infall halos are also likely to be anisotropic, and perhaps have alignments with the local tidal tensor. In this subsection, we investigate the alignments of the three eigenvectors of local tidal tensor with the position and velocity vectors of infall halos. The position vector,  $\mathbf{r}$ , of an infall halo is defined to be the vector from the minimum potential position of its host to the infall halo itself, while the velocity vector,  $\mathbf{v}$ , is defined to be its velocity relative to the velocity of the host. We use  $\theta_i^r$  ( $\theta_i^v$ ) to denote the angle between the position (velocity) vector and tidal eigenvector  $\mathbf{t}_i$  ( $i = 1, 2, 3$ ), i.e.

$$\cos(\theta_i^r) = \frac{\mathbf{r} \cdot \mathbf{t}_i}{|\mathbf{r}||\mathbf{t}_i|}; \quad \cos(\theta_i^v) = \frac{\mathbf{v} \cdot \mathbf{t}_i}{|\mathbf{v}||\mathbf{t}_i|}. \quad (3)$$

Here again, we first present the results for the staying population of the infall halos. Figure 8 shows the mean  $|\cos \theta_i^r|$  as a function of  $t_1$ . It can be seen that the position vectors have a strong

---

<sup>1</sup>Note that correlation does not necessarily imply causation unless other possibilities are exhausted. A proof of causation, therefore, needs a much more detailed analysis.

tendency to align with  $\mathbf{t}_1$  (the stretching direction) and to be perpendicular to  $\mathbf{t}_3$  (the compressing direction), and are almost uncorrelated with  $\mathbf{t}_2$ . According to the definition of the tidal field, the large scale mass distribution around a host halo tends to be in a filament along  $\mathbf{t}_1$  or within a sheet perpendicular to  $\mathbf{t}_3$ . Thus, the accretion mass flows towards the hosts are expected to be preferentially within these large scale structures, and the alignments shown in Figure 8 follow directly from this expectation. These results are consistent with that of Libeskind et al. (2014b), who found that mass accretion has the preference to be along the direction of the weakest collapse, which is the  $\mathbf{t}_1$  direction defined here. Comparing the black and green lines in Figure 8, we see that the average alignment signal is stronger for infall halos at higher redshift, particularly for low-mass hosts and for hosts located in high  $t_1$  regions. This is unexpected as the tidal tensor is estimated using halos at  $z = 0$ . One possible reason is that nonlinear effects, which tend to suppress alignment, are weaker at higher  $z$ . This interpretation is consistent with the fact that the alignments are weaker in higher  $t_1$  regions where nonlinear effects are expected to be stronger. Regardless its origin, this result suggests that our  $z = 0$  tidal field is a valid environmental indicator for halos at high redshift (at least to  $z \sim 1$ ).

Figure 9 show the mean  $|\cos \theta_v^i|$  as a function of  $t_1$ . Like  $|\cos \theta_i^r|$  shown in Figure 8,  $|\cos \theta_v^i|$  shows a strong correlation with the strength of the tidal force, and the dependence is stronger for low-mass hosts at low redshift. For example, for M12(S) at low redshift, there appears to be two different accretion patterns depending on the environment within which the host is embedded. In a weak tidal field, infall halos are preferentially accreted along the directions that are parallel with  $\mathbf{t}_1$  and perpendicular to  $\mathbf{t}_3$  (see the black solid lines in the left panels of Figure 8). The velocity vectors of these infall halos have a weak tendency to be parallel with  $\mathbf{t}_1$  but a strong tendency to be perpendicular to  $\mathbf{t}_3$ , as shown by the black solid lines in the left panels of Figure 9. In contrast, in a strong tidal field, infall halos are accreted along directions that are almost uncorrelated with the tidal tensor, while the velocity vectors tend to be perpendicular to  $\mathbf{t}_1$  and parallel with  $\mathbf{t}_3$ . For sample M13(S) and M13(S'), and for infall halos with high  $z_{\text{inf}}$ , the overall trends are very similar, albeit weaker.

The dependence on the tidal strength described above is interesting. In particular, why are the alignment signals stronger for host halos located in weak tidal field where large scale tidal field is expected to have a weak impact? The large scale (usually filamentary) structure surrounding a halo in a weak tidal field is not expected to be massive in comparison to the halo itself, and the thickness of the filamentary structure is likely to be comparable to the size of the halo (see Figure 10 for an example). For a host halo residing in a small filament, where the eigenvectors  $\mathbf{t}_1$  and  $\mathbf{t}_3$  are expected to be parallel with and perpendicular to the filament, respectively, the gravitational field is dominated by the host halo itself. The infall halos, which are located in the filament, are expected to have the tendency to move along the filament as they fall onto the host, so that the position and velocity vectors of the infall halos both have the tendency to be aligned with the filament. In this case, the role of the tidal field is to produce a ‘cold’ filamentary structure from which the halo accrete new material. In contrast, for halo located in a strong tidal field,

the surrounding structure is usually larger than the halo, even if it is a filamentary structure on a larger scale (see Figure 10). In this case, the halo can accrete infall halos from different directions, producing a weak alignment between the position vectors and the tidal eigenvectors. In such an environment, the large scale tidal field plays an important role in determining the motions of infall halos, which generates deceleration of accretion along  $\mathbf{t}_1$  and acceleration of accretion along  $\mathbf{t}_3$ . This explains why in a strong tidal field, the velocities of the infall halos tend to be parallel with  $\mathbf{t}_3$  and perpendicular to  $\mathbf{t}_1$  (Fig. 9), even though they still have a (weak) tendency to be distributed along  $\mathbf{t}_1$  at the time of accretion (Fig. 8).

The ejected halos exhibit similar dependence of  $|\cos\theta_i^r|$  on  $t_1$ . The mean alignment signal is weaker than that for the staying population, indicating that the ejected halos fall onto their hosts in a more isotropic manner. The difference between ejected and staying populations is particularly large in the velocities of infall halos, with the ejected population showing a much stronger tendency of their velocity vectors to be perpendicular to  $\mathbf{t}_1$  and parallel with  $\mathbf{t}_3$  in all environments. In the weak tidal field, this velocity - tidal field alignment for ejected halos is opposite to that for the staying population (Figure 9). These results together suggest that ejected halos are a special population of infall halos even before they are accreted by their hosts.

#### 4. Environmental Dependence of Halo Dynamical Properties

In the previous section we have shown that the accretion patterns of halos are correlated with the tidal field at  $z = 0$ . Since the intrinsic properties of dark matter halos are expected to depend on their formation histories, halo intrinsic properties are expected to be correlated with environment as well. Wang et al. (2011) have investigated the correlation between various halo structural properties with environment. Here we focus on the dynamical properties of dark matter halos, such as halo velocity structure and spin. There have been investigations about how the velocity anisotropy, spin and velocity ellipsoid of halos are affected by environment (e.g. Bett et al. 2007; Gao & White 2007; Hahn et al. 2007; Zhang et al. 2009, FW10). Our approach is different from these studies in that we use tidal field as an environmental indicator. More importantly, we try to interpret the environmental effect in terms of the environmental dependence of the accretion we obtained above.

We first investigate the velocity anisotropy parameter, which is defined to be

$$\beta = 1 - \frac{\sigma_\theta^2}{2\sigma_r^2}, \quad (4)$$

where  $\sigma_r$  and  $\sigma_\theta$  are, respectively, the radial and tangential velocity dispersion, evaluated using all halo particles. By definition, a negative (positive) value of  $\beta$  implies dominance of tangential (radial) motion, and  $\beta = 0$  indicates an isotropic velocity field. Figure 11 shows  $\beta$  as a function of  $t_1$  for host halos at  $z = 0$  in two mass ranges. There is a clear trend that  $\beta$  decreases monotonically with increasing  $t_1$ . The internal velocity fields are dominated by radial motion for halos in weak

tidal fields, and are almost isotropic for halos in strong tidal fields. FW10 found that halos of low  $\beta$  are more clustered than those of high  $\beta$ . Given that the tidal field is on average stronger in higher density regions (Wang et al. 2011), our results are consistent with theirs. Note that for a given  $t_1$ ,  $\beta$  is higher (meaning radial velocities is more dominating) for higher mass halos.

The velocity anisotropy of halos very likely reflects the anisotropy in the velocity distribution of infall halos. As a test of this, we calculate the mean cosine of the infall angle,  $\langle \cos \alpha_{\text{inf}} \rangle_{\text{H}}$ , weighted by the infall halo mass, for each host halo and show  $\beta$  versus  $\langle \cos \alpha_{\text{inf}} \rangle_{\text{H}}$  in Figure 12. Here, only staying infall halos are used to calculate  $\langle \cos \alpha_{\text{inf}} \rangle_{\text{H}}$ . We see a very strong positive correlation between these two quantities. The more tangential the mean orbit of the infall halos is, the more dominated the host halo is by tangential motions. Given the strong correlations between  $\cos \alpha_{\text{inf}}$  and  $t_1$  shown in Figure 7, the dependence of  $\beta$  on  $t_1$  is straightforward to understand.

To investigate the velocity anisotropy in more detail, we estimate the velocity anisotropy profile,  $\beta(r/r_{\text{vir}})$ , for individual host halos. Here  $r$  is the distance to the minimum potential position in the host halo, and  $r_{\text{vir}}$  is its virial radius. Here we use all particles in each radius bin to calculate the dispersion. Some non-halo particles may be included, but our test showed the effect is small. Figure 13 presents the results separately for halos residing in the highest, intermediate and lowest 20%  $t_1$  environments. For clarity, in each case, we only show the profiles of 2% halos randomly selected from the total sample. The median  $\beta$  profiles and the one sigma scatter are also plotted for reference. The large scatter in the innermost bins for the low mass halos are due to small number statistics. These profiles are in broad agreement with those obtained by Ludlow et al. (2011) from a much higher resolution simulation. As one can see from the right panels, the anisotropy profile depends significantly on the tidal field. For halos in the lowest 20 percentile of  $t_1$  distribution, the median  $\beta$  increases monotonously with increasing radius, indicating that the orbits of dark matter particles become increasingly radial as  $r$  increases. In contrast, for halos in the highest 20 percentile of  $t_1$ , the median  $\beta$  first increases and then decreases with  $r$ , reaching a maximum value of  $\beta \sim 0.2$  at  $r \sim 0.16r_{\text{vir}}$ . The velocity dispersion on average approaches isotropy ( $\beta \rightarrow 0$ ) in the outermost regions of such halos. The environmental effect decreases with decreasing radius, becoming unimportant at  $r < 0.1r_{\text{vir}}$ . In the innermost region, the velocity dispersion is quite isotropic (i.e.  $\beta \sim 0$ ), independent of the tidal field.

As shown in Zhao et al. (2003), a cold dark matter halo grows in an inside-out fashion after its potential well is established. Thus, the outer parts of halos are expected to be dominated by newly accreted material, and the material in the outer part should contain more information about the recent accretion events. This is the primary reason why the velocity structure in the outer parts of halos depends strongly on  $t_1$ . The behavior in the inner parts is more difficult to understand. As shown in Figure 7, radial accretion is actually more dominating at higher redshift. Since the inner parts are expected to have formed earlier, the weak anisotropy seen in the inner region cannot be due to the initial orbits of infall halos. It is possible that non-linear evolution, such as radial orbit instability (Carpintero & Muzzio 1995; MacMillan et al. 2006; Bellovary et al. 2008) have suppressed the initial velocity anisotropy. It is also possible that the early assembly of

halos is more dominated by major mergers, and the associated violent relaxation reduces the initial anisotropy (Lu et al. 2006).

Next we consider another important halo property, namely the angular momentum. Following common practice, we use the spin parameter,

$$\lambda = \frac{J|E|^{1/2}}{GM_0^{5/2}} \quad (5)$$

to characterize the angular moment of a halo, where  $J$  is the angular momentum,  $E$  the total energy and  $G$  the gravitational constant. We adopt the method presented in Bett et al. (2007) to estimate the total energy. The direction of the angular momentum (the spin direction) of a halo is denoted by  $\mathbf{j}$ .

Figure 14 shows the median  $\lambda$  as a function of  $t_1$ . Clearly, on average halos spin faster in a stronger tidal field, and the dependence is stronger for more massive halos. This result has already been obtained in Wang et al. (2011) and is consistent with the spin-dependent halo clustering found by Bett et al. (2007).

As shown in Figure 6, the tidal field can significantly enhance the tangential velocities of infall halos, which may in turn increase the orbital angular momenta of the host halo. To demonstrate this, we estimate the mean tangential velocity,  $\langle v_\theta/v_{\text{vir}} \rangle_{\text{H}}$ , of infall halos (the staying population only) for each  $z = 0$  host. Figure 15 shows how  $\lambda$  depends on  $\langle v_\theta/v_{\text{vir}} \rangle_{\text{H}}$ . As expected, the spin parameter has a strong positive correlation with the mean tangential velocity of infall halos. This suggests that halos acquire their angular momenta via the large scale tidal field which regulate the orbital angular momenta of infall halos.

In the literature, halo angular momenta are believed to be generated by tidal torques of the large scale structure (e.g. Porciani et al. 2002). One unique prediction of the tidal torque theory is that the halo spin axis tends to be parallel with the intermediate axis the tidal field, i.e.  $\mathbf{t}_2$ , and perpendicular to  $\mathbf{t}_1$  and  $\mathbf{t}_3$ . Wang et al. (2011) detected such alignments in their simulations, but the signals are rather weak (see also Forero-Romero et al. 2014). Some studies also found that halo spin tends to be perpendicular to filament and parallel to sheet (e.g. Hahn et al. 2007; Zhang et al. 2009; Libeskind et al. 2013b), which is consistent with the alignment with the intermediate axis of the tidal field. As we have already demonstrated in Section 3, accretion patterns are quite different between strong and weak tidal fields, and so the alignment signals may also vary with the strength of the local tidal field. To test this, we study the angle  $\zeta_i$  between  $\mathbf{j}$  and  $\mathbf{t}_i$ :

$$\cos(\zeta_i) = \frac{\mathbf{j} \cdot \mathbf{t}_i}{|\mathbf{j}||\mathbf{t}_i|} \quad (i = 1, 2, 3). \quad (6)$$

Figure 16 shows the mean of  $|\cos \zeta_i|$  as a function of  $t_1$ . As one can see, when the tidal field is weak, the alignments are perfectly consistent with the prediction of the tidal torque theory, in that  $\mathbf{j}$  tends to align with  $\mathbf{t}_2$ . However, as the tidal field gets stronger, the alignments become weaker and weaker. For small halos in regions of high  $t_1$ , the trend is eventually reversed so that the spin tends

to be aligned with  $\mathbf{t}_1$  and perpendicular to  $\mathbf{t}_2$ . This reversal is caused by the strengthened tidal truncation of accretion along the  $\mathbf{t}_1$  direction where the tearing by the tidal field is the strongest. In an analysis of spin alignments using all halos (or galaxies) without regarding their local tidal fields, the opposite trends in strong and weak fields may cancel each other and weaken the total signal. It is thus important to take into account the local tidal field strength when investigating spin alignments in both observation and numerical simulation.

Finally, we examine the second moment tensor of the internal velocity field of a halo, defined as

$$I_{jk}^v = \sum_n v_{n,j} v_{n,k}, \quad (7)$$

where  $v_{n,j}$  ( $j = 1, 2, 3$ ) are the three velocity components of the  $n$ th particle in the halo. The square root of the eigenvalues of the tensor can be used to represent the principal axes,  $I_1^v$ ,  $I_2^v$  and  $I_3^v$  ( $I_1^v \geq I_2^v \geq I_3^v$ ), and the axis ratios, such as  $I_3^v/I_1^v$ , to characterize the velocity ellipsoid. The corresponding eigenvectors,  $\mathbf{I}_1^v$ ,  $\mathbf{I}_2^v$  and  $\mathbf{I}_3^v$ , represent the directions of the major, intermediate and minor axes of the velocity ellipsoid, respectively.

To check the alignment between the eigenvectors of the velocity tensor and the tidal field, we use the angle  $\phi_i^v$  defined as

$$\cos(\phi_i^v) = \frac{\mathbf{I}_i^v \cdot \mathbf{t}_i}{|\mathbf{I}_i^v| |\mathbf{t}_i|} \quad (i = 1, 2, 3). \quad (8)$$

Figure 17 shows the mean of  $|\cos \phi_i^v|$  as a function  $t_1$ . In weak tidal field,  $\mathbf{I}_1^v$  tends to be parallel with  $\mathbf{t}_1$ , but an opposite trend is seen in strong tidal field. The trend in  $|\cos \phi_3^v|$  is very similar but slightly weaker, and there is no significant alignments between  $\mathbf{I}_2^v$  and  $\mathbf{t}_2$  regardless of tidal field strength. The transition is similar to what is seen in the relationship between  $\cos \theta_i^v$  and  $t_1$  (see Section 3.3), and it may be possible that the results shown in Figure 17 can be understood in terms of halo accretion. As shown in Figure 9, the velocities of infall halos tend to be parallel with  $\mathbf{t}_1$  and perpendicular to  $\mathbf{t}_3$  in weak tidal field. If the host halo retains the velocity structure of the infall halos, the major (minor) principal axes of its velocity ellipsoid are expected to be parallel with  $\mathbf{t}_1$  ( $\mathbf{t}_3$ ), as shown in Figure 17. Similarly, the different accretion pattern at high  $t_1$  can also explain why  $\mathbf{I}_1^v$  ( $\mathbf{I}_3^v$ ) tends to be perpendicular to  $\mathbf{t}_1$  ( $\mathbf{t}_3$ ) in strong tidal fields.

It is interesting to see how the velocity ellipsoid in the inner halo regions, where galaxies are located, are aligned with the local tidal field. To do this, we calculate the alignment between the tidal field and the velocity ellipsoid of the halo particles within some radius  $r$ . The dashed curves in Figure 17 show the results for  $r = 0.1r_{\text{vir}}$ , and the averages of  $|\cos \phi_i^v(< r/r_{\text{vir}})|$  are shown as functions of  $r/r_{\text{vir}}$  in Figure 18. It is evident that the velocity ellipsoids of the inner halo regions align with the tidal field in a different way from the whole halos. In weak tidal fields, the alignment signals in the inner regions are slightly weaker than those for the whole halos. In strong tidal field, however, the alignments of the inner ellipsoids on average are opposite to the whole halo. For example, for low mass halos, the major and minor principal axes of the inner velocity ellipsoids tend to be parallel with  $\mathbf{t}_1$  and  $\mathbf{t}_3$ , respectively, but they tend to be perpendicular to each other for

the whole halos. This suggests that the accretion pattern at early epoch is similar to that in weak tidal field environments at low redshift.

## 5. Discussion and Summary

In this paper, we investigate the environmental dependence of halo accretion and their impact on the halo dynamical properties. We construct halo merger trees from  $N$ -body simulations and identify infall halos that are about to merge with their hosts. The infall halos are divided into two populations: the staying population which remain as subhalos within their hosts at  $z = 0$ ; the ejected population which are ejected by their hosts at presented day. We use the large scale tidal field estimated from the halo population at  $z = 0$  as environmental indicator.

We first investigate the infall halo mass functions in various tidal fields. The mass function for the staying population is quite independent of both the tidal field and host halo mass. In contrast, the ejected halo mass function depends strongly on the tidal field. In a stronger tidal field, infall halos are more easily ejected by their hosts at  $z = 0$ , and smaller infall halos are more likely to be ejected than massive ones.

We then check the dependence of the orbital parameters of infall halos on local tidal field. The tidal field does not significantly affect the average radial velocities of infall halos, but can generate tangential motions. Consequently, infall halos in stronger tidal fields tend to have higher mean tangential velocities, larger infall angles and higher velocity dispersions. These results suggest that tidal field tends to pull the accretion flow into the orbit of the host and enhance the velocity dispersion among the infall halos, making the accretion flow ‘hotter’ and more difficult to capture by the host.

We find that the accretion patterns are different between strong and weak tidal fields. In weak tidal fields, the positions of infall halos relative to their hosts have a strong tendency to be parallel with the stretching direction of the tidal field,  $\mathbf{t}_1$ , and perpendicular to the compressing direction,  $\mathbf{t}_3$ . Similarly, the velocities tend to be parallel with  $\mathbf{t}_1$  and perpendicular to  $\mathbf{t}_3$ . The situation in strong tidal fields is rather different, or even the opposite: the alignments between the position and tidal vectors become weaker or even absent, and the velocities tend to be perpendicular to  $\mathbf{t}_1$  and parallel with  $\mathbf{t}_3$ . Such difference is particularly strong for infall halos at low redshift around low-mass hosts.

The ejected population shows very different behavior from the staying population. They have much higher tangential velocities. In particular, the velocities have a strong tendency to be perpendicular to  $\mathbf{t}_1$  and parallel with  $\mathbf{t}_3$  in both weak and strong tidal fields. Ejected halos are more abundant in stronger tidal fields because the larger and more tangential velocities generated by the tidal forces make the infall halos more difficult to hold by their hosts.

The environmental effects of halo accretion are imprinted on the halo dynamical proper-

ties. The environmental dependence of infall angles results in a correlation between the velocity anisotropy and tidal field. In particular, the large scale tidal field can affect the anisotropy down to radius much smaller than the virial radius. Tidal field increases the tangential velocities of infall halos, producing a positive correlation between halo spin and the strength of local tidal field. The alignment signal of spin with tidal field is different between weak and strong tidal fields; only in weak tidal fields does the spin-tidal field alignment follow the prediction of the tidal torque theory, with the spin parallel to the intermediate axis and perpendicular to the major axis of the tidal tensor, while in strong fields the alignment is the opposite, at least for low-mass halos. Finally, we find a dramatic transition in the alignment between the principal axes of halo velocity ellipsoid and the tidal field tensor in strong and weak tidal field, A radial dependence for this alignment is also found, which differs between weak and strong tidal fields. All these indicate that large scale tidal field affects halo dynamical properties via regulating the flow patterns around halos.

Our results suggest the tidal field describes well the following two aspects of environmental effects. First, strong tidal field (i.e. larger  $t_1$ ) tends to make the surrounding environment ‘hotter’, thereby boosting the fraction of the ejected sub-halos, and increasing the tangential component of velocity and the velocity dispersions. This affects halo dynamical properties, making the internal velocity field less radial and boosting the angular momentum in a way that is different from the predictions of the tidal torque theory. Second, the local tidal field describes well the local density and velocity structures from which material is accreted in halos, which in turn explains how halo intrinsic properties are correlated with local tidal fields.

Our results have important implications for observations. For example, our results suggest that the correlation between spin axes of disk galaxies and the large scale structure should be studied separately for the weak and strong tidal fields. The fact that strong alignments of halo velocity ellipsoids with local tidal fields extend all the way to halo central parts suggests that the orientations of elliptical galaxies should be tightly correlated with the local tidal fields. The predicted dependence of such alignments on the strength of local tidal fields can also be tested using a large sample of elliptical galaxies. Furthermore, the infall patterns around halos can be studied by using the distributions and velocity fields traced by satellite galaxies in and around dark matter halos represented by galaxy groups. Since the tidal fields enhance the tangential velocities of infall halos, we may expect the dynamical time scales relevant to mergers to be larger for those located in stronger tidal fields. This difference in dynamical time scales may lead to differences in the abundance and properties of the satellite population. We will come back to some of these problems in our future work.

### Acknowledgments

We thank Volker Springel for kindly providing his SUBFIND code. The numerical calculations have been done on the supercomputing system in the Supercomputing Center of University of Science and Technology of China. This work is supported by the Strategic Priority Research

Program "The Emergence of Cosmological Structures" of the Chinese Academy of Sciences, Grant No. XDB09010400, NSFC (11421303), 973 program (2015CB857005), the Fundamental Research Funds for the Central Universities, HJM would like to acknowledge the support of NSF AST-1109354.

## REFERENCES

- Allgood B., Flores R. A., Primack J. R., Kravtsov A. V., Wechsler R. H., Faltenbacher A., Bullock J. S., 2006, MNRAS, 367, 1781
- Bahé Y. M., McCarthy I. G., Crain R. A., Theuns T., 2012, MNRAS, 424, 1179
- Bellovary J. M., Dalcanton J. J., Babul A., Quinn T. R., Maas R. W., Austin C. G., Williams L. L. R., Barnes E. I., 2008, ApJ, 685, 739
- Benson A. J., 2005, MNRAS, 358, 551
- Bett P., Eke V., Frenk C. S., Jenkins A., Helly J., Navarro J., 2007, MNRAS, 376, 215
- Carpintero D. D., Muzzio J. C., 1995, ApJ, 440, 5
- Colín P., Klypin A. A., Kravtsov A. V., 2000, ApJ, 539, 561
- Dalal N., White M., Bond J. R., Shirokov A., 2008, ApJ, 687, 12
- Davis M., Efstathiou G., Frenk C. S., White S. D. M., 1985, ApJ, 292, 371
- Desjacques V., 2008, MNRAS, 388, 638
- Fakhouri O., Ma C.-P., 2009, MNRAS, 394, 1825
- Faltenbacher A., White S. D. M., 2010, ApJ, 708, 469
- Forero-Romero J. E., Contreras S., Padilla N., 2014, MNRAS, 443, 1090
- Gao L., Springel V., White S. D. M., 2005, MNRAS, 363, L66
- Gao L., White S. D. M., 2007, MNRAS, 377, L5
- Gao L., White S. D. M., Jenkins A., Stoehr F., Springel V., 2004, MNRAS, 355, 819
- Giocoli C., Tormen G., van den Bosch F. C., 2008, MNRAS, 386, 2135
- Hahn O., Porciani C., Carollo C. M., Dekel A., 2007, MNRAS, 375, 489
- Jiang L., Cole S., Sawala T., Frenk C. S., 2014, arXiv:1409.1179
- Jing Y. P., Suto Y., Mo H. J., 2007, ApJ, 657, 664

- Keselman J. A., Nusser A., 2007, MNRAS, 382, 1853
- Lacerna I., Padilla N., 2011, MNRAS, 412, 1283
- Lacerna I., Padilla N., 2012, MNRAS, 426, L26
- Li R., Gao L., Xie L., Guo Q., 2013, MNRAS, 435, 3592
- Li Y., Mo H. J., Gao L., 2008, MNRAS, 389, 1419
- Libeskind N. I., Hoffman Y., Forero-Romero J., Gottlöber S., Knebe A., Steinmetz M., Klypin A., 2013a, MNRAS, 428, 2489
- Libeskind N. I., Hoffman Y., Gottlöber S., 2014a, MNRAS, 441, 1974
- Libeskind N. I., Hoffman Y., Steinmetz M., Gottlöber S., Knebe A., Hess S., 2013b, ApJ, 766, L15
- Libeskind N. I., Knebe A., Hoffman Y., Gottlöber S., 2014b, MNRAS, 443, 1274
- Lu Y., Mo H. J., Katz N., Weinberg M. D., 2006, MNRAS, 368, 1931
- Ludlow A. D., Navarro J. F., Springel V., Jenkins A., Frenk C. S., Helmi A., 2009, ApJ, 692, 931
- Ludlow A. D., Navarro J. F., White S. D. M., Boylan-Kolchin M., Springel V., Jenkins A., Frenk C. S., 2011, MNRAS, 415, 3895
- Maulbetsch C., Avila-Reese V., Colín P., Gottlöber S., Khalatyan A., Steinmetz M., 2007, ApJ, 654, 53
- MacMillan J. D., Widrow L. M., Henriksen R. N., 2006, ApJ, 653, 43
- Mo H. J., White S. D. M., 1996, MNRAS, 282, 347
- Mo H., van den Bosch F. C., White S., 2010, Galaxy Formation and Evolution
- Navarro J. F., Frenk C. S., White S. D. M., 1995, MNRAS, 275, 56
- Porciani C., Dekel A., Hoffman Y., 2002, MNRAS, 332, 325
- Rasia E., Tormen G., Moscardini L., 2004, MNRAS, 351, 237
- Sandvik H. B., Möller O., Lee J., White S. D. M., 2007, MNRAS, 377, 234
- Sparre M., Hansen S. H., 2012, J. Cosmology Astropart. Phys., 10, 49
- Springel V., 2005, MNRAS, 364, 1105
- Springel V., White S. D. M., Tormen G., Kauffmann G., 2001, MNRAS, 328, 726
- Tormen G., 1997, MNRAS, 290, 411

- Vitvitska M., Klypin A. A., Kravtsov A. V., Wechsler R. H., Primack J. R., Bullock J. S., 2002, ApJ, 581, 799
- Wang H., Mo H. J., Jing Y. P., 2009a, MNRAS, 396, 2249
- Wang H., Mo H. J., Jing Y. P., Yang X., Wang Y., 2011, MNRAS, 413, 1973
- Wang H., Mo H. J., Yang X., van den Bosch F. C., 2012, MNRAS, 420, 1809
- Wang H. Y., Jing Y. P., Mao S., Kang X., 2005, MNRAS, 364, 424
- Wang H. Y., Mo H. J., Jing Y. P., 2007, MNRAS, 375, 633
- Wang Y., Yang X., Mo H. J., van den Bosch F. C., Katz N., Pasquali A., McIntosh D. H., Weinmann S. M., 2009b, ApJ, 697, 247
- Wechsler R. H., Bullock J. S., Primack J. R., Kravtsov A. V., Dekel A., 2002, ApJ, 568, 52
- Wechsler R. H., Zentner A. R., Bullock J. S., Kravtsov A. V., Allgood B., 2006, ApJ, 652, 71
- Wetzel A. R., 2011, MNRAS, 412, 49
- Wetzel A. R., Tinker J. L., Conroy C., Bosch F. C. v. d., 2014, MNRAS, 439, 2687
- Yang X., Mo H. J., van den Bosch F. C., Jing Y. P., 2005, MNRAS, 356, 1293
- Yang X., Mo H. J., van den Bosch F. C., Pasquali A., Li C., Barden M., 2007, ApJ, 671, 153
- Yang X., Mo H. J., Zhang Y., van den Bosch F. C., 2011, ApJ, 741, 13
- Zhang Y., Yang X., Faltenbacher A., Springel V., Lin W., Wang H., 2009, ApJ, 706, 747
- Zhao D. H., Jing Y. P., Mo H. J., Börner G., 2009, ApJ, 707, 354
- Zhao D. H., Mo H. J., Jing Y. P., Börner G., 2003, MNRAS, 339, 12

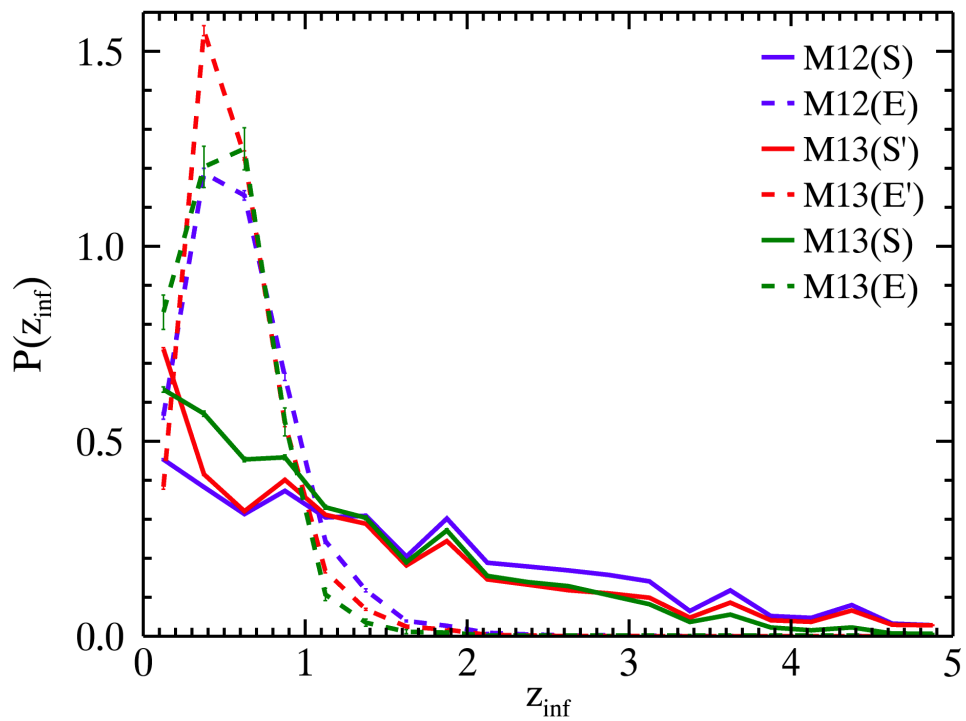


Fig. 1.— The probability distribution of infall redshift,  $z_{\text{inf}}$ , for the six infall halo samples as indicated in the figure. See Section 2.2 for sample selections.

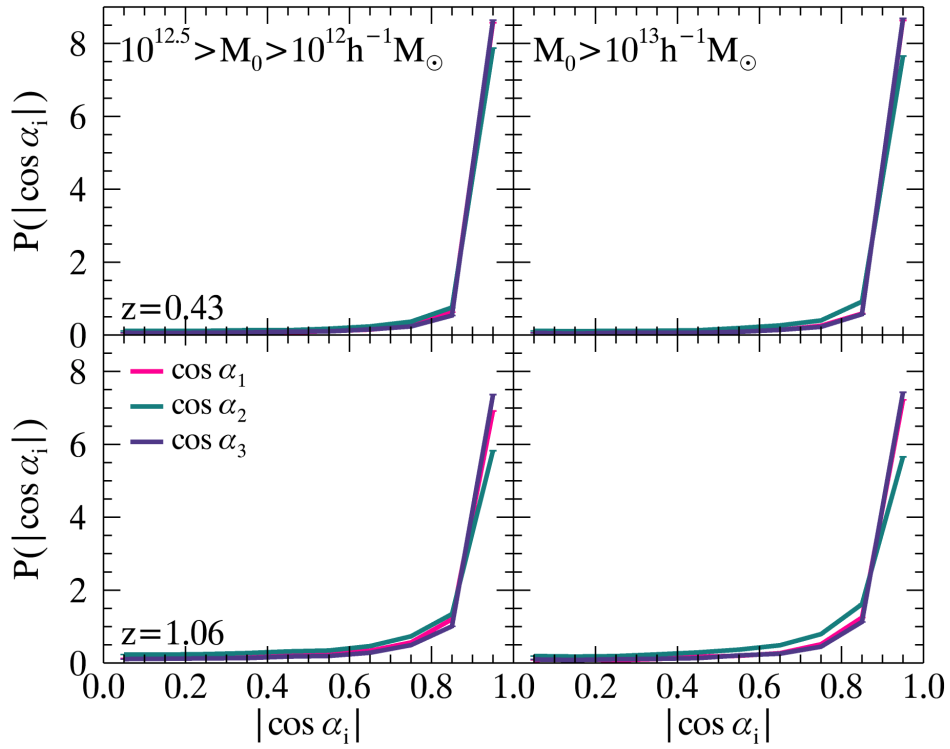


Fig. 2.— The probability distributions of  $|\cos \alpha_i|$ , where  $\alpha_i$  is the angle between the eigenvectors  $\mathbf{t}_i$  ( $i = 1, 2, 3$ ) of the tidal field around a  $z = 0$  halo and the corresponding eigenvectors around its main progenitors at  $z = 0.4$  (upper panels) and  $z = 1.0$  (lower panels). The right and left panels show the results for Milky Way sized and massive group sized halos, respectively.

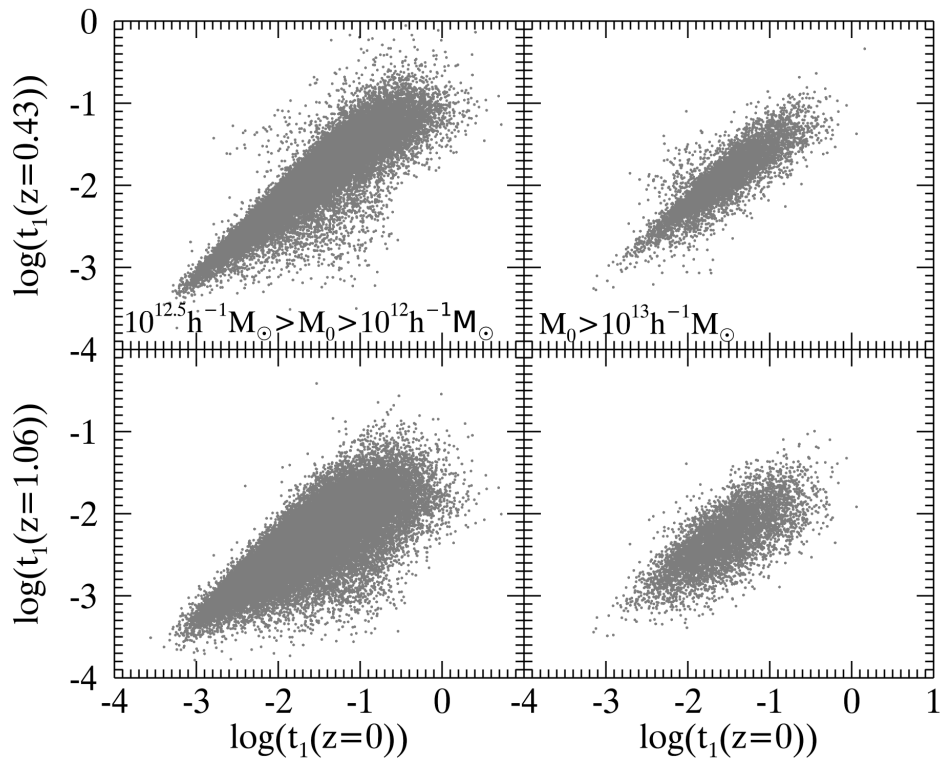


Fig. 3.— The comparison between the tidal field strength ( $t_1$ ) around a  $z = 0$  halo and that around its main progenitors at  $z = 0.4$  (upper panels) and  $z = 1.0$  (lower panels). The right and left panels show the results for Milky Way sized and massive group sized halos, respectively.

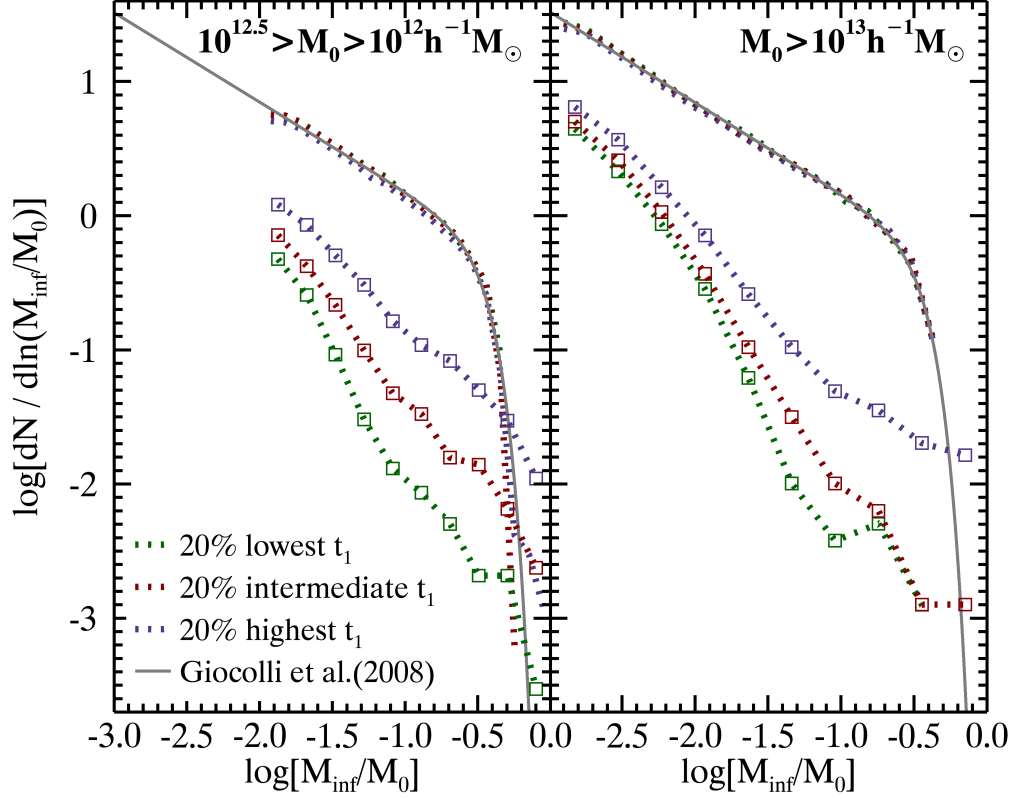


Fig. 4.— The comparison of infall halo mass functions in different environments. The blue, red and green lines correspond to the host halos in the lowest, intermediate, and highest 20 percentiles of  $t_1$ . The left panel shows the results for host halos of  $10^{12.5} \geq M_0 \geq 10^{12} h^{-1} M_\odot$ , and the right panel shows the results of  $M_0 \geq 10^{13} h^{-1} M_\odot$ . The dotted lines show the staying population of infall halos. Note that the results for the three  $t_1$  samples almost overlap. The dotted lines connecting squares are for ejected halos. The gray lines are the best-fitting results based on the function given by Giocoli et al. (2008).

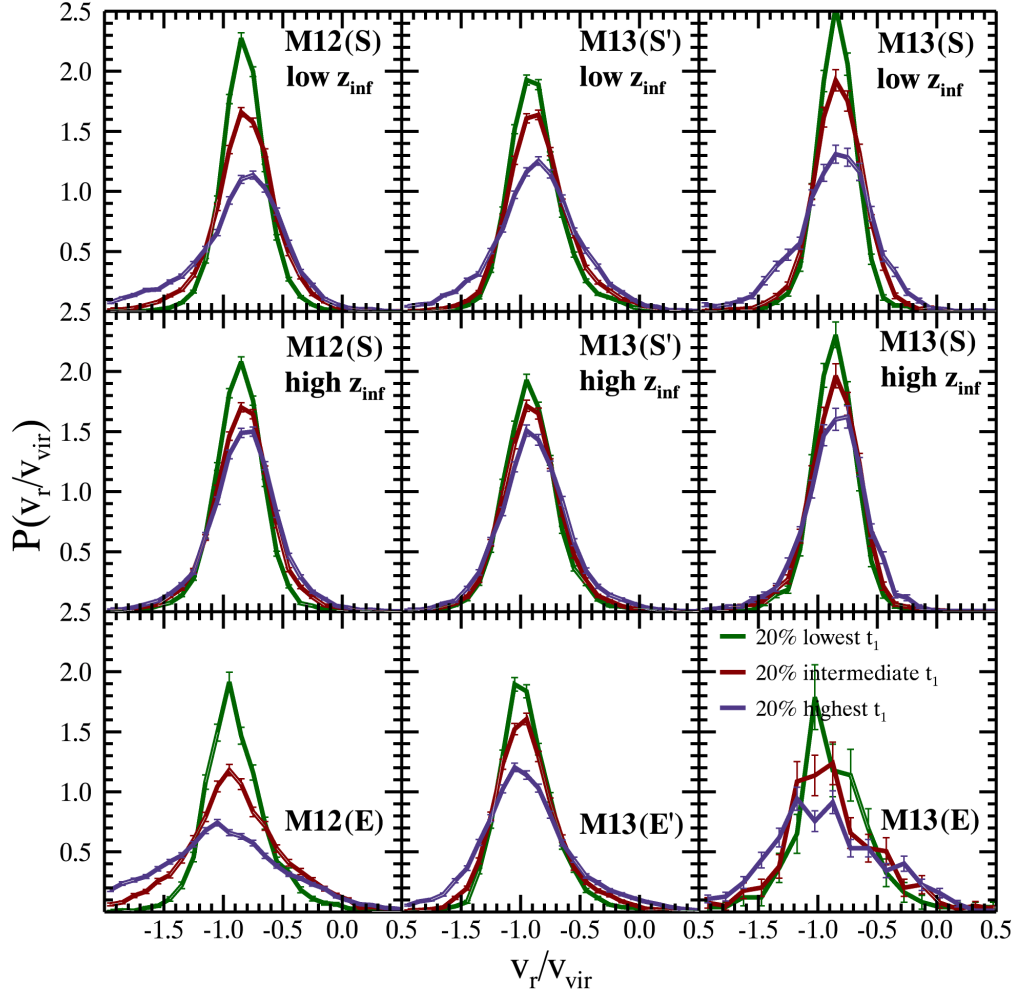


Fig. 5.— The radial velocity distributions of infall halos in different environments. The blue, red and green lines show the results for host halos in the lowest, intermediate and highest 20 percentiles of  $t_1$ . Results are shown for infall halos in two different redshift ranges, as indicated in each panel. The velocity is normalized by  $v_{\text{vir}}$ , the virial velocity of the host halo at the infall redshift. The error bars are Poisson errors.

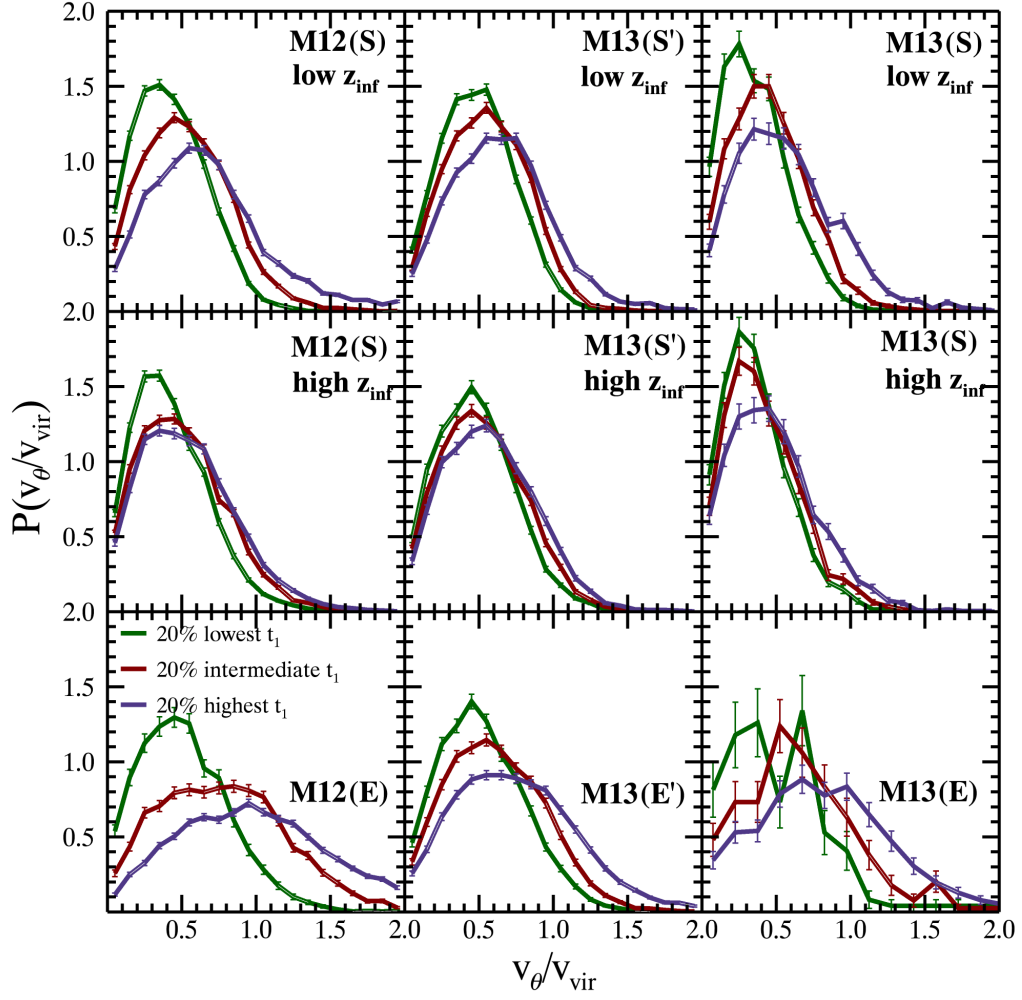


Fig. 6.— The same as Figure 5 but for the tangential component of the infall velocity.

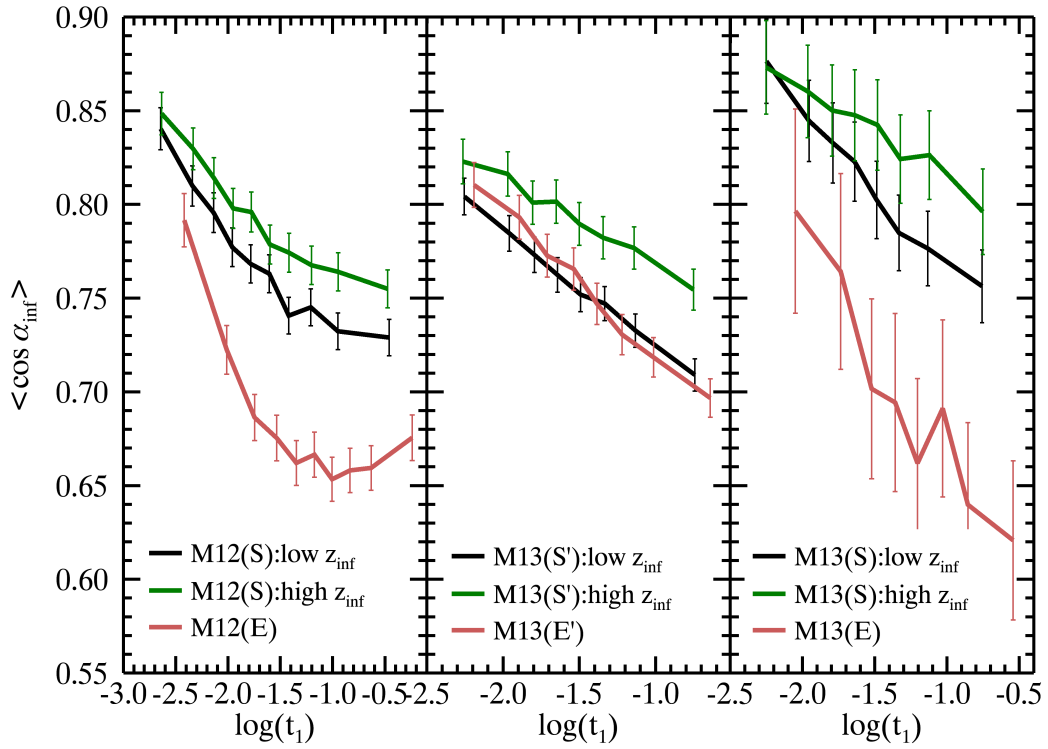


Fig. 7.— The mean cosine of the infall angle  $\alpha_{\text{inf}}$ , defined in equation (2), as a function of the tidal field strength,  $t_1$ , for different samples as indicated in the panels. For each curve, the  $t_1$  bin sizes are chosen so that each bin contains the same number of halos. The error bars are Poisson errors.

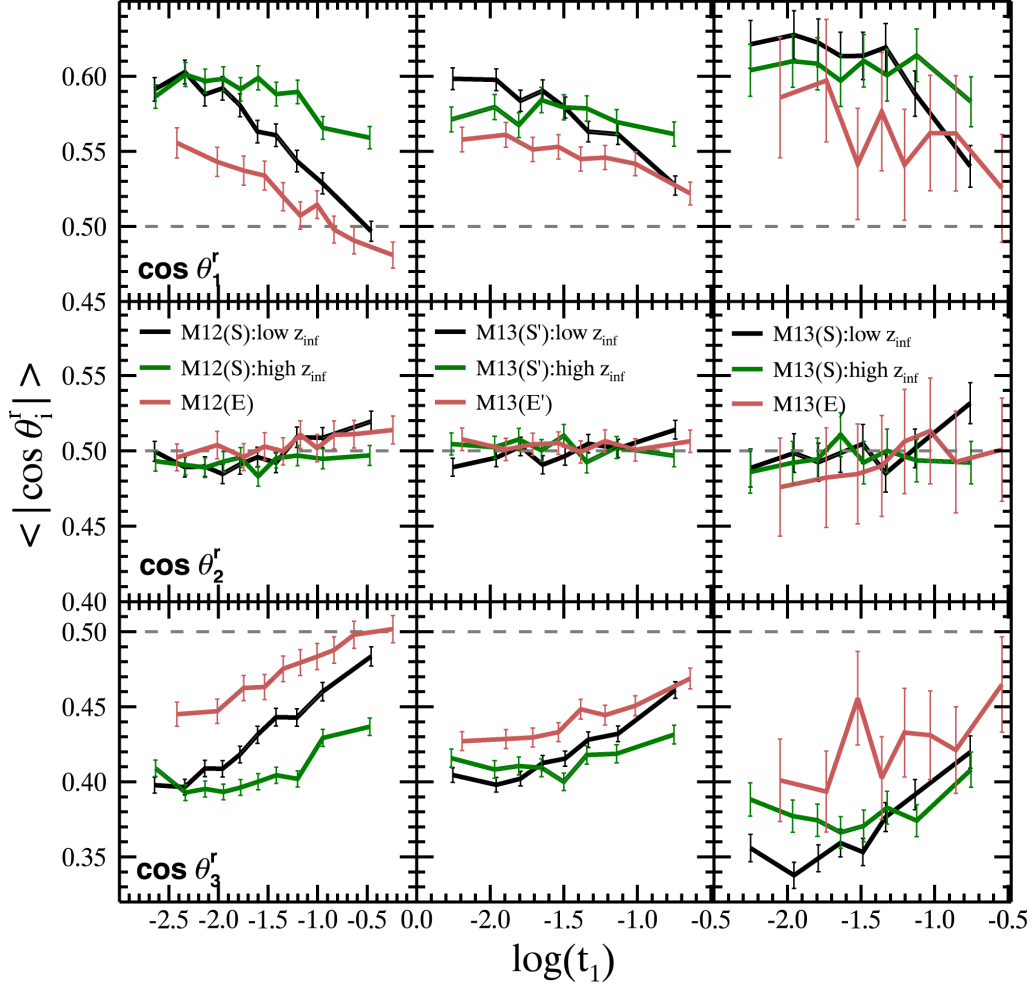


Fig. 8.— The mean of  $|\cos \theta_i^r|$  ( $i = 1, 2, 3$ ) defined in equation (3), as a function of  $t_1$ . From top to bottom, results are shown for  $i = 1$  (major axis),  $i = 2$  (intermediate axis) and  $i = 3$  (minor axis). From left to right, results are shown for different samples as indicated in the intermediate-row panels. The dashed lines indicate isotropic distribution. The error bars are Poisson errors.

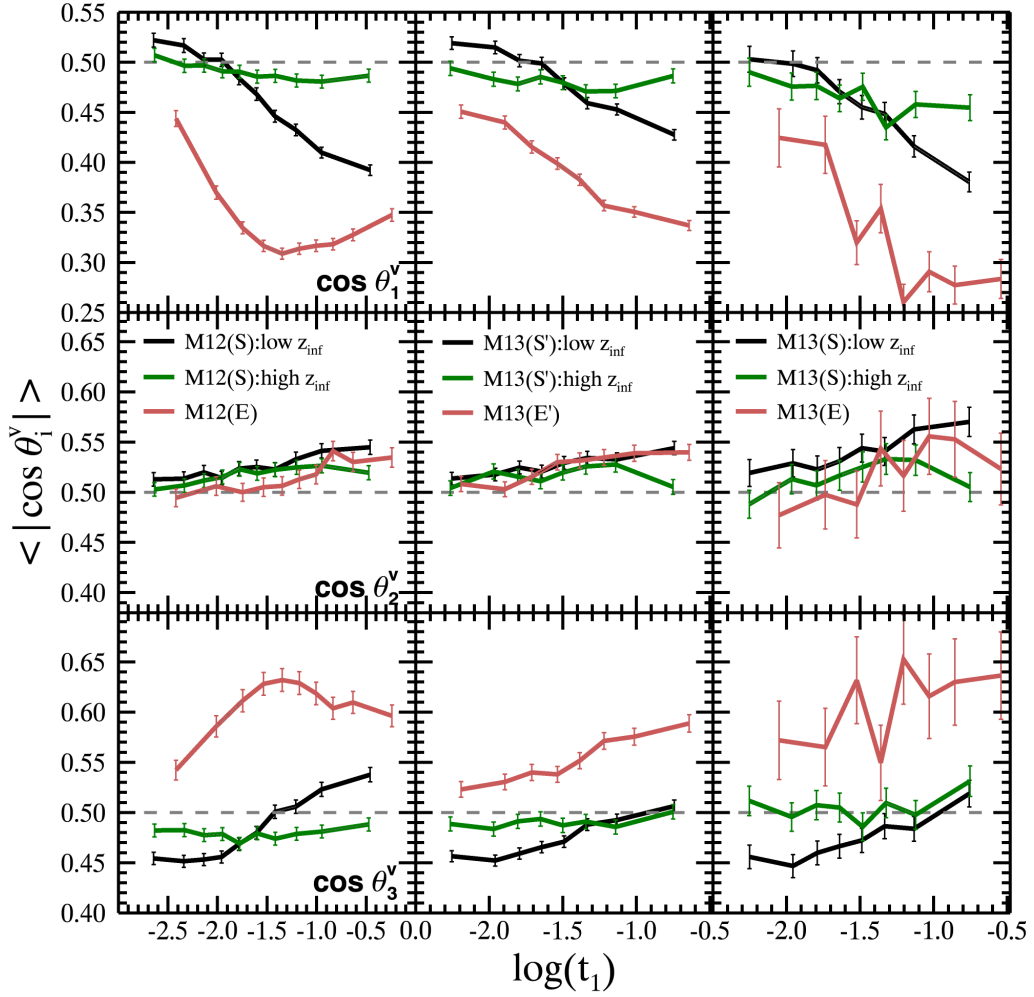


Fig. 9.— The same as Figure 8 but for  $\theta_i^v$ , defined in equation (3).

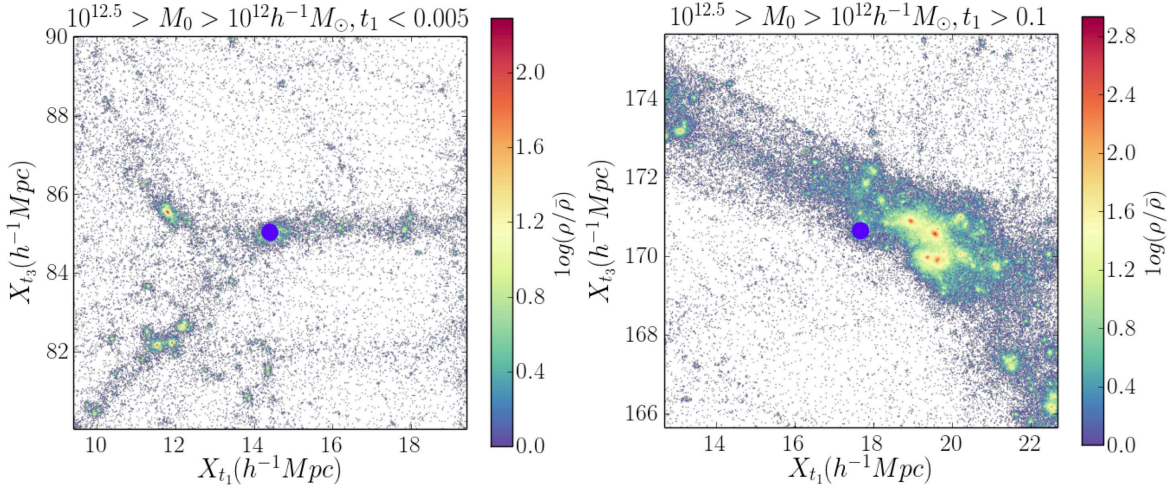


Fig. 10.— The projected density contrast maps around two Milky Way sized halos in weak and strong tidal fields as indicated in the panels. The two halos are shown as blue solid circles at the centers of the panels. The maps are shown in the  $t_1$ -  $t_3$  plane, and the thickness is  $5h^{-1}\text{Mpc}$ . The values of the density contrast are color coded, as shown in the color bars.

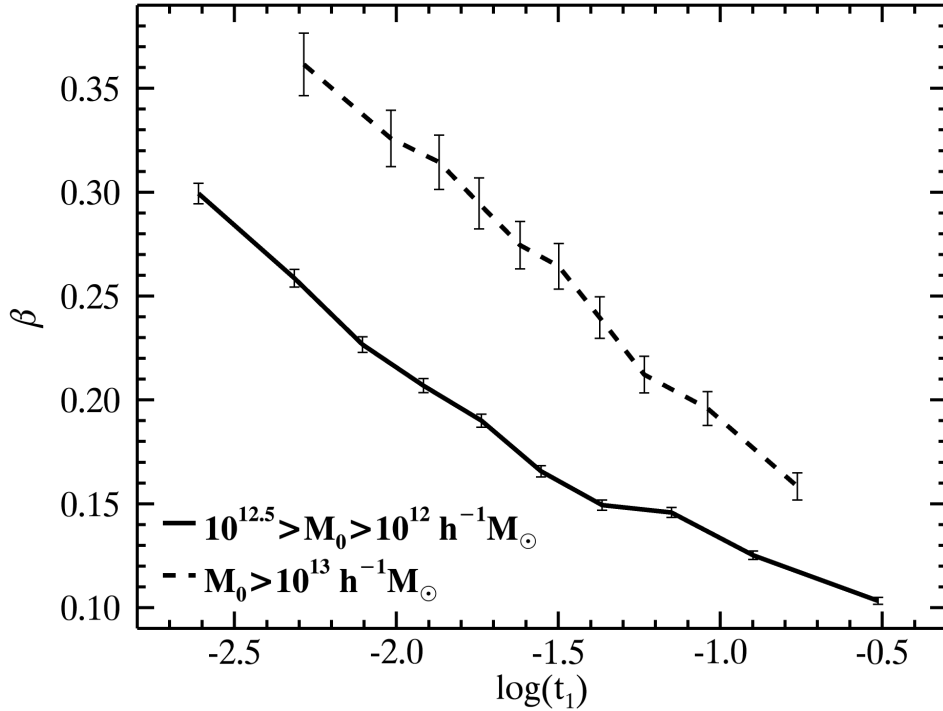


Fig. 11.— The correlation between velocity anisotropy,  $\beta$  defined in equation (4), of host halos and  $t_1$  for two mass ranges. All  $t_1$  bins contain equal number of halos. The curves connect the median values of  $\beta$ , while the error bars are Poisson errors.

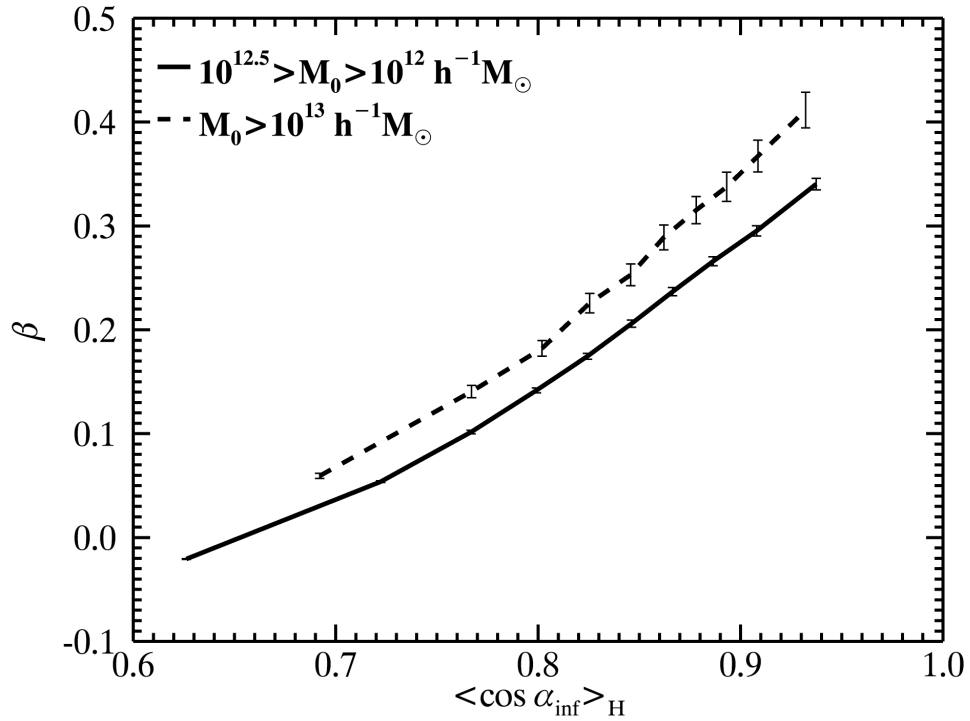


Fig. 12.— The correlation between the velocity anisotropy  $\beta$  and  $\langle \cos \alpha_{\text{inf}} \rangle_{\text{H}}$ . For each host halo,  $\langle \cos \alpha_{\text{inf}} \rangle_{\text{H}}$  is the mass-weighted average value over all of its infall halos in the staying population. All  $\langle \cos \alpha_{\text{inf}} \rangle_{\text{H}}$  bins contain equal number of halos. The curves connect the median values of  $\beta$ , while the error bars are Poisson errors.

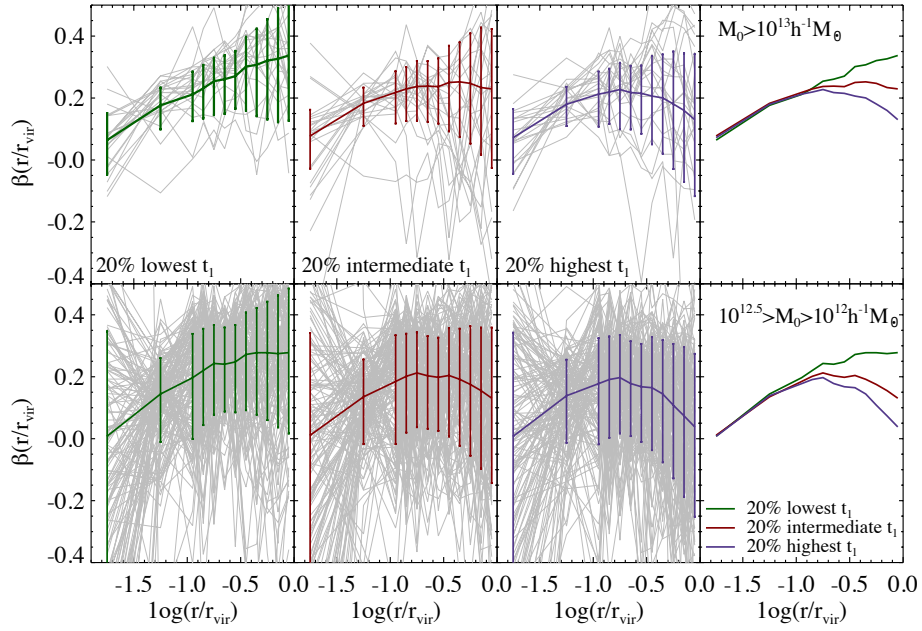


Fig. 13.— The velocity anisotropy profiles (gray lines) for  $z = 0$  host halos in different tidal fields, as indicated in the panels. For clarity, profiles of 2% of the halos in each sample are plotted. The median profiles are plotted in colored lines, with error bars representing the  $1\sigma$  scatter. For comparison, the median profiles for different  $t_1$  are re-plotted in the rightest-hand column.

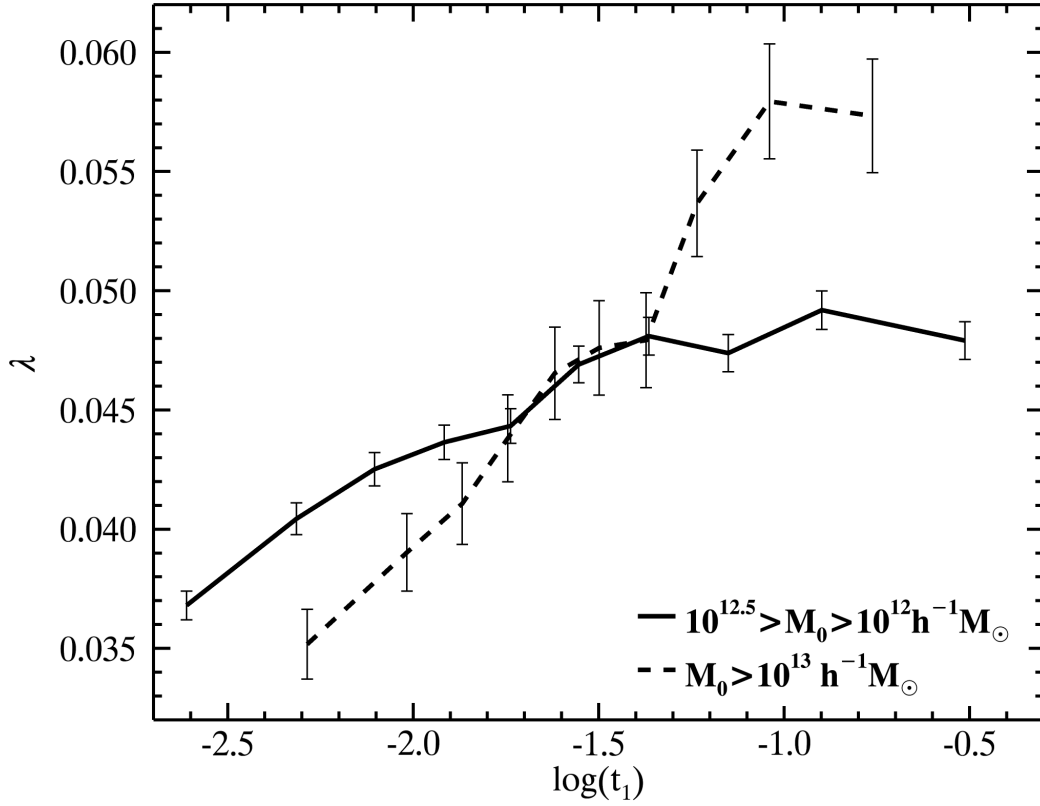


Fig. 14.— The spin parameter,  $\lambda$  defined by equation (5), of host halos as a function of  $t_1$ . All  $t_1$  bins contain equal number of halos. The curves connect the median values of  $\lambda$ , while the error bars are Poisson errors.

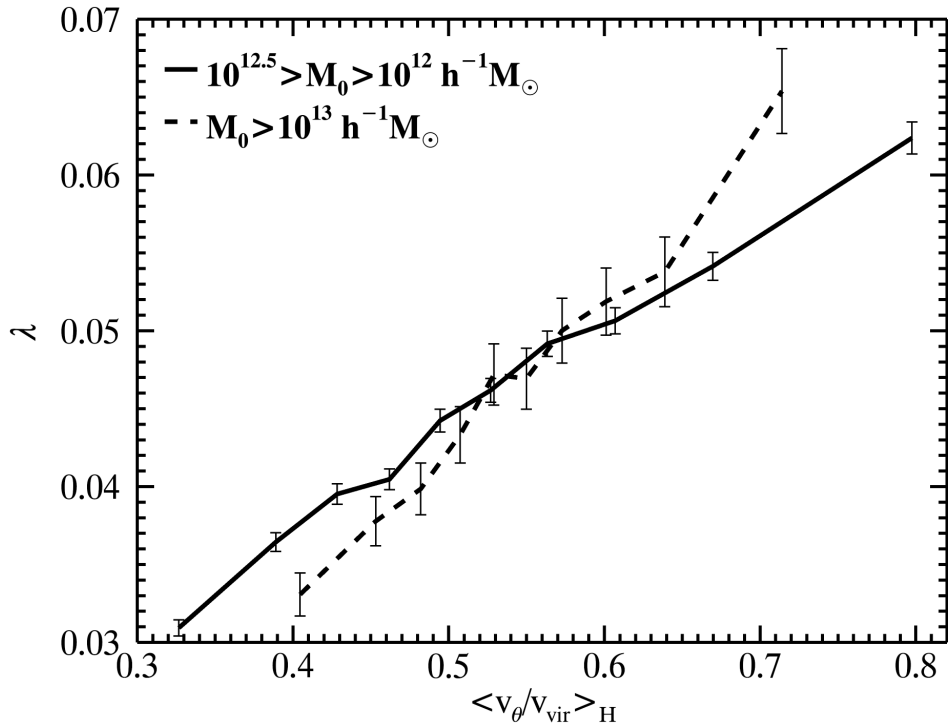


Fig. 15.— The spin parameter,  $\lambda$ , as a function of  $\langle v_\theta/v_{\text{vir}} \rangle_{\text{H}}$ . For each host halo,  $\langle v_\theta/v_{\text{vir}} \rangle_{\text{H}}$  is the mass-weighted average value over all of its infall halos in the staying population. All  $\langle v_\theta/v_{\text{vir}} \rangle_{\text{H}}$  bins contain equal number of halos. The curves connect the median values of  $\lambda$ , while the error bars are Poisson errors.

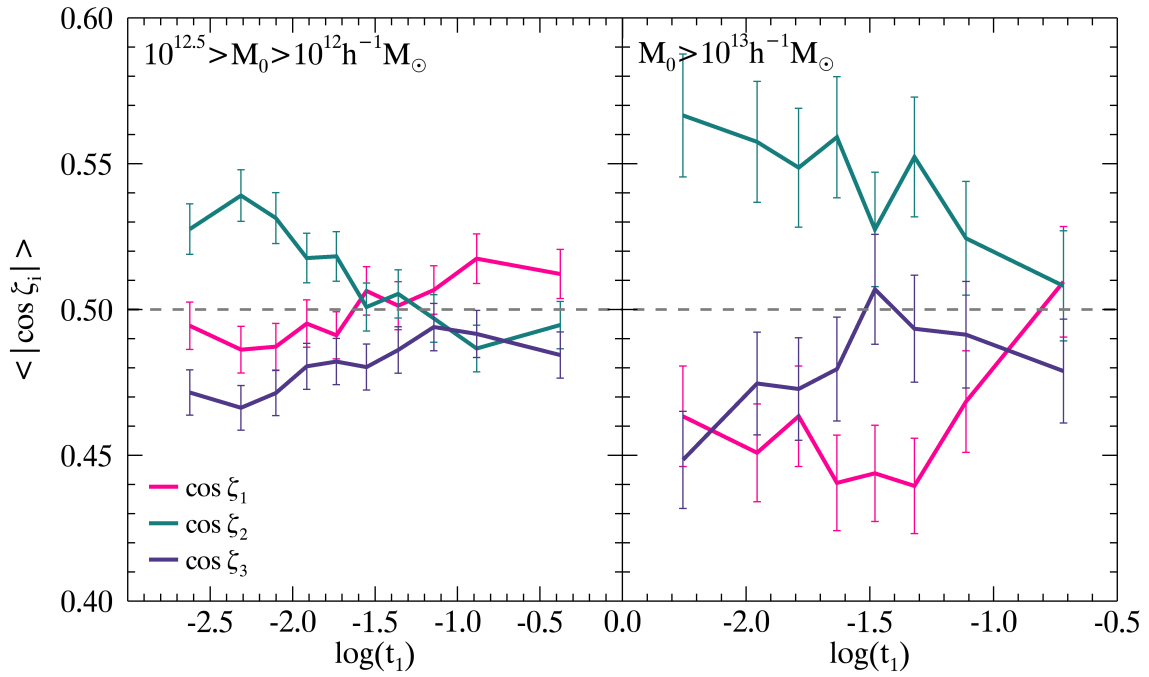


Fig. 16.— The mean of  $|\cos \zeta_i|$ , a measure of the alignment between the tidal field and halo spin defined by equation (6), as a function of tidal field strength  $t_1$ . All  $t_1$  bins contain equal number of halos. The error bars are Poisson errors. The horizontal lines indicate no alignment.

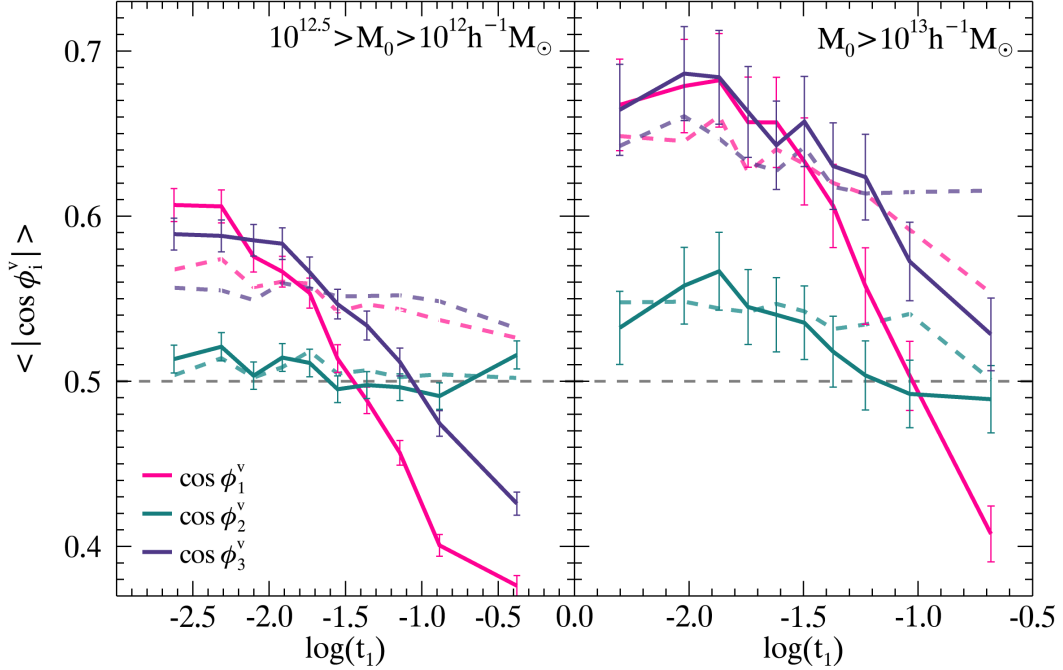


Fig. 17.— The mean of  $|\cos \phi_i^v|$ , defined by equation (8), as a function of  $t_1$ . All  $t_1$  bins contain equal number of halos. The solid lines are obtained from using all particles in a halo, while the dashed lines use halo particles in the inner part with  $r \leq 0.1 r_{vir}$ . The Poisson errors, which are the same for both the solid and dashed curves at a given  $t_1$ , are shown only on the solid curves. The horizontal lines indicate isotropic distribution.

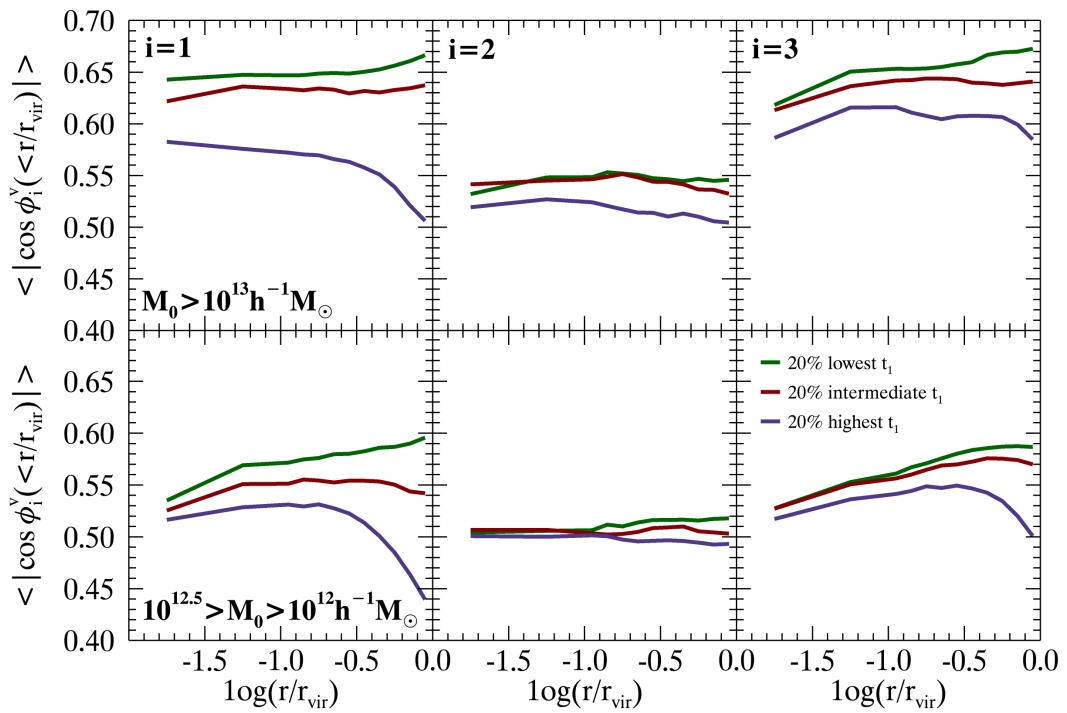


Fig. 18.— The mean alignment profile within individual halos located in tidal fields of three different  $t_1$  20 percentile intervals. Here  $|\cos \phi_i^v(< r/r_{vir})|$  measures the alignment between tidal field tensor and velocity ellipsoids obtained using particles within  $r/r_{vir}$ .